AN EXPERIMENTAL STUDY OF THE EFFECT OF RESHOCK ON THE

INCLINED INTERFACE RICHTMYER-MESHKOV INSTABILITY

A Thesis

by

SKYLAR ANTHONY CREEL

Submitted to the Office of Graduate and Professional Studies of
Texas A&M University
in partial fulfillment of the requirements for the degree of

MASTER OF SCIENCE

Chair of Committee,	Devesh Ranjan
Committee Members,	Sharath Girimaji
	Je-Chin Han
Head of Department,	Andreas A. Polycarpou

May 2014

Major Subject: Mechanical Engineering

ABSTRACT

An experimental study of the Richtmyer-Meshkov instability (RMI) is presented here for the twice-shocked, or reshocked, inclined interface perturbation. Experiment work was conducted in the shock tube facility in the Advanced Fluid Mixing Lab at Texas A&M University. Experimental cases were performed at a single Atwood number (0.23), Mach number (1.55) and inclination angle (60°) with a perturbation amplitude-to-wavelength ratio of 0.29. Mie scattering and particle image velocimetry (PIV) data was collected using a planar laser system and was used to compute mixing width, vorticity and circulation.

Experimental cases were defined by the time which the interface was allowed to develop before reshock interaction. Cases 1, 2 and 3 were defined for development times of 1.635 ms, 3.5 ms and 5.105 ms respectively. Developmental time series were created using Mie scattering images from multiple experimental runs for each case and mixing width data was derived from the time series images. Interface growth rates post-reshock are computed using mixing width and interface length measurements. PIV data for pre- and post-reshock times were used to create vorticity plots for a qualitative discussion of the effect of reshock on the interface and estimate the circulation deposited on the flow field by reshock. Results indicate that the longer the initial interface is allowed to develop prior to reshock interaction, the greater the circulation post-reshock and change in circulation across the reshock interaction. Turbulent kinetic energy

spectra for all cases are computed as well as the turbulent length scales of the flow based on mixing width, circulation and interface length.

DEDICATION

To my wife and best friend, Melissa. I would not be where I am today or achieved what

I have achieved without her love and support.

ACKNOWLEDGEMENTS

TABLE OF CONTENTS

LIST OF FIGURES

x

LIST OF TABLES

1. INTRODUCTION

The Richtmyer-Meshkov instability (RMI) [1], [2] is a hydrodynamic instability that is driven by the misalignment of a pressure gradient and a density gradient. The RMI is closely related to the Rayleigh-Taylor instability (RTI)[3], [4] as well as the Kelvin-Helmholtz instability (KHI) [5], [6]. While the RTI is driven by a small constant acceleration and the KHI is driven by shear along the fluid interface, the RMI is driven by an impulsive acceleration usually in the form of a shock wave. The effect of this misalignment can be seen in the baroclinic term of the vorticity equation (1.1).

$$\frac{D\bar{\omega}}{Dt} = \bar{\omega}\cdot\bar{\nabla}\bar{u} + \nu\nabla^2\bar{\omega} + \left[\frac{1}{\rho^2}\bar{\nabla}\rho\times\bar{\nabla}P\right]_{\text{Baroclinic Term}} \tag{1.1}$$

The gradients within the baroclinic term can be represented by dimensionless quantities that provide more description of the conditions the instability is created from. The pressure gradient and by extension the acceleration can be defined by the Mach number of the shock wave that will be interacting with the fluid interface, defined in equation (1.2),

$$M = \frac{V}{\sqrt{\gamma RT}} \tag{1.2}$$

Where M is the Mach number, V is the velocity of the shock wave and $\sqrt{\gamma RT}$ is the speed of sound in the gas through which the shock wave is travelling. The shock wave is created by the pressure difference in different parts of the shock tube which will be discussed in greater detail later. The shock wave imparts an instantaneous velocity

increase and with it an impulsive acceleration. The density gradient is created by different fluids or the same fluid with different conditions meeting at the interface and can be concisely described using the Atwood number, defined in equation (1.3), where the subscripts h and l represent the heavy and light fluids respectively.

$$A = \frac{\rho_h - \rho_l}{\rho_h + \rho_l} \tag{1.3}$$

The most prominent method for conducting experiments involving the RMI is currently using a shock tube facility. Other experimental methods will be detailed in section II of this work. A shock tube is an experimental facility that creates a shock wave through the use of a high pressure volume that is separated from a low pressure volume. The high pressure volume is known as the driver and the low pressure volume is called the driven section and is often followed by a test section where data is acquired. By rupturing the separating diaphragm, gas rushes from the high pressure volume in the form of compression waves that will coalesce into a plane shock wave given enough distance in the low pressure section. In a paired process to the compression that moves into the low pressure section, expansion waves travel into the high pressure volume to maintain continuity. Shock tube facilities may or may not be constructed with an end wall at the end of the test section (driven section). If the facility has an end wall the shock wave will reflect off of the bottom wall and interact with the fluid interface for a second time. This second interaction is called reshock and, similar to the initial shock wave, will create more baroclinic vorticity, thus driving the interface further towards a turbulent state.

The leading motivation for the study of the RMI can be found in the work currently being performed by the National Ignition Facility (NIF). NIF is currently performing experiments in an attempt to produce a net gain of energy from inertial confinement fusion (ICF). ICF seeks to produce energy through the fusion of fuel made up of Deuterium and Tritium by compressing the fuel pellet to pressures and temperatures necessary to fuse the fuel. NIF uses 192 high-powered lasers to compress the fuel. The energy cost of these lasers must be overcome by the energy produced by the fusion but currently the yield of the fusion reaction is being limited by mixing that occurs between the high density fuel and the lower density coatings that are placed around the fuel target. The target coating is ablative and transmits the impact of the laser on the coating to the fuel as a shock wave. The RMI is introduced into the ICF process through the interaction pressure gradient created by the laser compression and the density gradient that is present at the interface of the fuel and ablative coating. The misalignment between the gradients can be provided by perturbations in the coating surface as well as the shock wave; the shock wave perturbations caused by its origin as 192 point sources. The RMI created vorticity causes mixing between the coating and the fuel which dilutes the fuel into a less pure state, reducing the output from the process. By understanding more about the development of the RMI in many different situations and using the understanding to predict and eventually control the mixing that occurs, the yield of ICF can be increased in an effort to provide a cleaner, more efficient energy alternative to those that are currently employed today.

1.1 Literature Review

In an effort to provide an in-depth context for the work presented, previous contributions to this research topic will be presented. The previous work will be divided into two sections focusing on the theoretical works and the simulations and experimental work. Because of the dependence of reshock on the effects of the initial shock wave, previous work pertaining to studies of the reshocked RMI as well as the once-shocked RMI will be presented.

1.1.1   Theoretical Works

The theoretical work on the RMI began with the work of Richtmyer [2], that was based on Taylor's previous work [4] and Meshkov [1]. Richtmyer investigated the case where the acceleration present in the RTI was impulsive in nature and derived that the growth rate of perturbation amplitude was dependent on the initial perturbation wavelength and amplitude, the acceleration and the Atwood number. Using this relation, Richtmyer assumed compressible effects could be neglected and used a Dirac delta function to model the impulsive acceleration. These assumptions led him to find that the interface growth rate was proportional to the velocity jump created by the impulsive acceleration. Richtmyer used these new developments to perform computer simulations of a sinusoidal fluid interface that was accelerated by a shockwave. The results showed good agreement with the theory at early time though not perfect. A decade later, Meshkov was able to validate the theoretical work of Richtmyer though his own experimental work, but problems with the experiments produce an error greater than 10% when compared to the theory predicted values for growth rate. Meshkov's

experiments allowed him to add a prediction of the post-shock amplitude of the interface to Richtmyer's work.

Richtmyer's model would come to be known as the Richtmyer impulsive model and showed that the initial interface growth rate would be constant with time. Though this model remains important to the calculation of the growth of the instability, many researchers have modified and expanded this model in the time since its inception. The use of the average of the pre- and post-shock interface amplitudes be used along with the post shock Atwood number were proposed by Meyer and Blewett [7] after they performed numerical simulations based on the experimental work of Meshkov. The effect of compressibility on the instability's post-shock amplitude and the model was studied by Fraley [8] and Wouchuk and Nishihara [9]–[11] respectively and it was determined that compressibility effects were important within a certain range of growth. The aforementioned versions of Richtmyer's model were only valid for the light over heavy condition of the instability because under the heavy over light condition a phase inversion would occur causing the perturbation to dampen, invert and being to grow opposite of its initial amplitude. In an effort to account for this, Vandenboomgaerde *et al.* [12] developed a form of the impulsive model that would be valid for both the heavy over light and light over heavy conditions. In another addition to the model, Motl *et al.*[13] proposed a growth reduction factor for a diffuse interface that was in part based on experiments done by Brouillette and Sturtevant [14]

The validity of the impulsive model is strongly affected by whether the interface perturbation is linear or nonlinear. A perturbation is said to be linear if the amplitude to

wavelength ratio, η/λ, is less than 0.1. Some initial perturbations in Meshkov's work were inadvertently nonlinear and the results from those initial conditions proved to be in higher disagreement to Richtmyer's model. Linear perturbations are typically defined to have an amplitude-to-wavelength ratio less than 0.1 [15]. Work investigating the effect of nonlinearity has been performed by Aleshin *et al.* [16] as well as McFarland *et al.* [17]. Paramount to understanding nonlinear growth models is to define the substructures of the interface known as the bubble and the spike. The substructures names were first adopted during the observation of RTI development where in the mixing region wide areas of light fluid would penetrate the heavy fluid as thin protrusions of heavy fluid would travel into the light fluid. The growth rate of the interface is defined as the sum of the growth rates for each of the substructures. For cases where the Atwood number is greater than zero, the spike growth rate is larger than the bubble growth rate. For the linear case, work by both Zhang and Sohn [18], and Velikovich and Dimonte [19] utilized the method of Padé approximates to expand the model through addition of higher order terms. The work of Zhang and Sohn predicts the growth rate will stall then decline at later times. A review of the nonlinear theories for the RMI was presented by Holmes *et al.*[20] and showed good agreement between the models but pointed out the heightened disagreement at higher Mach Numbers.

The theoretical works presented thus far have focused on the interface development stemming from the interaction of the initial shock wave. As this work will be focused on what happens to the interface after it has been shocked for a second time, works that have developed models for the reshocked RMI will now be presented.

Models dealing with the growth rate of the interface post-reshock are still in the early stages of development due to the complex structure of the interface before the reshock wave interacts with the interface as will be seen in later sections of this work. The change in growth rate pre-reshock and post-reshock was studied by Mikaelian [21]. Mikaelian applied a potential flow model of a single-mode perturbation to a growing perturbation as would be the case after the perturbation had been shocked once. Many factors were studied to determine whether the second shock would accelerate, decelerate, stagnate or invert the perturbation and what criteria would cause each outcome. Brouillette and Sturtevant in their work with Richtmyer's model determined how it could be applied to a multi-shock system, but were only successful in maintaining accuracy if the interface amplitude at reshock is much smaller than the wavenumber[14]. Mikaelian later developed an empirical model applied to a multi-mode 3D pre-reshock perturbation that used experimental data to determine certain correctional constants [22].

1.1.2   Simulations and Experimental Work

Beyond the theoretical work presented in the previous section, studies of the RMI have been performed both experimentally and through computer simulations. These two approaches will be considered together because of the impact advances in either approach has on its counterpart. Experimental approaches to the RMI can be categorized by coordinate system, perturbation methodology and impulsive acceleration methodology.

The coordinate systems that are most available to the study of the RMI are 2D and 3D rectangular and converging 3D spherical. Experiments using the converging 3D

spherical system typically use high-powered lasers to induce the impulsive acceleration and examples include those currently underway at the National Ignition Facility (NIF) [23] at Lawrence Livermore National Laboratory (LLNL). The National Ignition Facility is a prime example of the integrated progress of simulations and experiments. While experiments are being developed and performed, researchers at LLNL, LANL, and other labs are working on computer simulations to assist in developing more advanced models to provide direction to further experiments. These simulations will be discussed later within this section and more information about the work being performed at NIF will be presented in section 1.2.

Use of rectangular geometry allows for more options when choosing acceleration and perturbation methods for experiments. There are three ways that have been used previously to the necessary impulsive acceleration: laser ablation, facility acceleration and mechanical acceleration. The use of lasers was discussed in relation to the 3D spherical experiments previously. The beam from one or more high-powered lasers impacts an ablative material and the force is transmitted as a shock through the adjacent material. This method produces strong shock waves but requires large amounts of power making and uses small length scales which make it an unlikely choice for most experimental designs. Laser-driven experiments can be used to study RTI [24] and KHI [25] as well as RMI [26].

Another method of generating the impulsive acceleration is to accelerate the facility itself. This can be accomplished by allowing a tank containing stratified fluid to fall into contact with a spring that will accelerate the tank upward [27]. Other methods

have been used to accelerate the tank include rockets [28] and linear electric motors [29] and using air pressure in opposition to gravity allows for study of the RTI as well [30]. The final acceleration production method that will be discussed is use of a shock wave. This method is the basis for shock tube facilities such as the one used for the experiments in this work. In a shock tube, a high-pressure volume is separated from a low-pressure volume by a diaphragm. By rupturing the diaphragm, compression waves from the high-pressure volume travel into the low-pressure volume and coalesce into a planar shock front if the shock tube is of adequate length. If the shock tube facility is constructed with a downstream end wall, the shock wave can reflect off of its surface and interact with the fluid interface a second time, a process called reshock. The importance of reshock to the study of the RMI will be discussed in greater detail in the next section.

Similar to the varied methods of inducing the necessary pressure gradient, the misaligned density gradient can be generated in many ways. It should be noted that it is also possible to alter the shock wave to create the misalignment as in the work of Vetter and Sturtevant [31][32]. The method used in Meshkov's seminal work, and in many works since, created the misaligned density gradient by shaping a thin membrane that separated the fluids into a designed shape [1]. This method provides a repeatable interface but when the shock wave interacts with the membrane remnants can be accelerated with the flow field and obscure optical diagnostics [31], [33]. An adaptation of the membrane experiments is to use a fluid film to shape the fluid interface as used in shock bubble interaction experiments [34]. The shock bubble experiments allow for

9

study of the RMI in a light-heavy-light or heavy-light-heavy configuration depending on the relationship between the fluids inside and outside of the soap bubble.

In an attempt to remove the interference created by the membrane material, experiments were designed that did not require the membrane to maintain the fluid interface. One membraneless method employs a plate to separate the fluids which is removed prior to the shock interaction [35]. This method imbeds small shear perturbations on the fluid interface as the plate is removed. A cylindrical interface can be created by dropping a column of heavy gas through a light gas, a method developed by Jacobs [36]. Multiple gas cylinders can be arranged to create a gas curtain to study the RMI for a light-heavy-light interface [37]. When the gas curtain perturbation is used, the light-heavy RMI and heavy-light RMI are coupled and develop in tandem. A planar interface can be created by co-flowing light and heavy gas into the shock tube from the top and bottom respectively and allowing the gases to exit the tube through ports at the desired interface location. Additional perturbations can be introduced to the co-flow interface by shaking the facility [38], creating shear along the interface [39] or oscillating pistons on the exit ports [13].

The method employed in this work is the inclined interface perturbation. It is similar to the planar co-flow method discussed previously in that the light and heavy gases are simultaneously injected into the facility. The facility itself is inclined from vertical such that gravity causes the heavy fluid to remain below the light fluid creating a scenario where the fluid interface is not perpendicular to the shock tube walls. This perturbation is very repeatable, as documented by the author in McFarland *et al.*[40] ,

and allows the cross product in the baroclinic term of the vorticity equation to be controlled by adjusting the facility inclination angle. The inclined interface has been studied in simulation by McFarland *et al.*[17] and a model predicting the circulation imparted on the interface by the shock wave has been developed my Samtaney and Zabusky [41], [42]. Similar interfaces have been studied in experiments such as the light-heavy-light chevron [43].

Now that work concerning the interaction of the initial shock and interface has been discussed, a review of the work focused on the reshock RMI can be presented. The purpose of studying reshock's influence on the interface is that the reflected wave imparts more vorticity into the flow field and increases mixing which drive the RMI towards a more turbulent state. Experiments focused on the reshocked RMI have been performed by Vetter and Sturtevant [31], Liu *et al.* [44] and Balasubramanian *et al.* [37] among many others [38], [45]–[48]. The purpose of studying reshock's influence on the interface is that the reflected wave imparts more vorticity into the flow field and increases mixing which drive the RMI towards a more turbulent state. The work presented is comparable to the work performed by Leinov *et al.* [33] who also studied the effect that different reshock interaction times had on the mixing zone of the interface by changing the bottom wall material and distance. Many have performed simulations that were focused on the RMI reshock. Using the initial conditions of the experiments performed by Collins and Jacobs [38], Latini *et al.* [49] performed simulations on the same experiments to study the effect of model order and grid resolution on the ability to accurately predict the experimental results. A further look into the experiments was

performed by Schilling *et al.* [50] focusing on the physics of reshock and the mixing and applying the circulation model developed by Samtaney and Zabusky [41], [42]. The simulations of Latini and Schilling were performed using weighted essentially non-oscillatory (WENO) methods. Other simulations have been performed using large-eddy simulation methods by Lombardini *et al.* [51] and Hill *et al.* [52]. Simulations on the reshock RMI are very computer-intensive and are constantly pushing the limitations of currently available hardware. As hardware and simulations are pushed by reshock, the ability of the simulations to predict mixing from the RMI increases. The progress of experiments and simulations are interconnected and driven further by study of the reshock RMI.

1.2 Applications

The RMI occurs in nature as well as man-made situations and is present in many areas of science and on scales large and small. In astral phenomena, large clouds of gas are influenced by shock waves stemming from supernovae causing density inhomogeneity to accelerate and mix [53]. These interactions have been shown to be a possible method for star formation [54] by creating significant mixing of gases of different temperatures and densities [55]. The RMI is applied in supersonic combustion by utilizing the increased mixing created by the shock wave interaction with the air fuel mixture. This interaction is the basis for scram jets and has been studied experimentally and computation to investigate the use of new fuels [56]–[58]. The RMI is also a factor in the medical field where it is used to break up gallstones and kidney stones or damage tumors [59].

The application that is the strongest motivator for research into the RMI is the development of inertial confinement fusion (ICF). With the world's population on the rise, and with it the energy demands of the world, new sources of energy are becoming more important by the day. Once ICF has advanced beyond its current efficiency, it could provide a clean source of power with abundant fuel and reduce the need for oil and other carbon-based fuels.

In ICF a fuel target is compressed to high temperatures and pressures to facilitate the creation of larger elements. For the experiments currently being performed at NIF, the fuel target is made up of Deuterium and Tritium [60] which fuses to create Helium when compressed. This fusion reaction releases a large amount of energy in the form of free neutrons which can be slowed down in water or other materials to harness the energy or used to create more fuel for fission reactors. This method allows for energy production on a very large scale, through ICF and breeding new fission fuel, from elements that are readily available in ocean water.

Current developmental work in ICF is being done at the National Ignition Facility at Lawrence Livermore National Lab. In their work, the fuel target is compressed through the use of 192 high-powered lasers in a semi-spherical array that provides upwards of 1.8MJ or 500 trillion watts. The fuel target is placed within a gold hohlraum that that will absorb the laser energy and emit x-rays into the fuel and provide uniform heating to the Beryllium ablative shell on the fuel. The lasers are fired in four pulses to control the compression rate of the fuel and timing of the shocks created from the ablative material [23]. The ablative material and the fuel are of different densities

and when coupled with the compression shocks provide the necessary conditions for the RMI to develop. The mixing caused by the instability alters the purity of the fuel which reduces the energy yield of the reaction. The need to understand and control this harmful mixing is a critical step in advancing ICF to the level necessary to become a viable power source.

1.3 Section Outline

The remainder of this work will present the experimental work performed by the author as well as an analysis of the results. The experimental section will be divided into sub-sections as follows: (1) a description of the experimental facility and data acquisition systems, (2) shock tube operating procedures will be detailed, (3) and finally the results of the experimental campaign will be presented.

2. EXPERIMENTAL FACILITY

This section will detail the components of the shock tube facility at the Texas A&M University advanced fluid mixing lab, shown in Figure 1, and the data acquisition systems that are currently in place. The shock tube at the TAMU advanced fluid mixing lab is a variable angle shock tube that is capable of operation in a horizontal (0°), vertical (90°), or any other orientation between. The shock tube facility at TAMU is made up of four main structural sections: the driver, the diaphragm loader, the driven section and the test section. These sections are supported by a wide flange I-beam (W12x40) that allows for sections to be manipulated while the tube is inclined and is also a mounting point for other hardware such as gas lines and the winch that separates the diaphragm loader to allow diaphragms to be changed. The tube is anchored by a large pivot assembly to a 64 cubic feet cement block, weighing approximately 45 kN, that isolates the tube from the foundation of the lab. The shock tube is modular in design so that the major sections of the facility can be rearranged to allow for greater flexibility in future experiment design. An in depth discussion of the sections of the shock tube is discussed in the first part of this section and is followed by a discussion of the data acquisition systems in use with the facility.

Driver wench
Hoist point
Diaphragm loader
Driver

Total length: ~9m
Driver length: 1.5m
Driven length: ~7.5m
Cross section:
~11.4cm x 11.4cm
θ: 0-90°
Max M: ~3.0

Driven Sections

Support I-beam

Interface creation section
Test section
Blank section

Windows
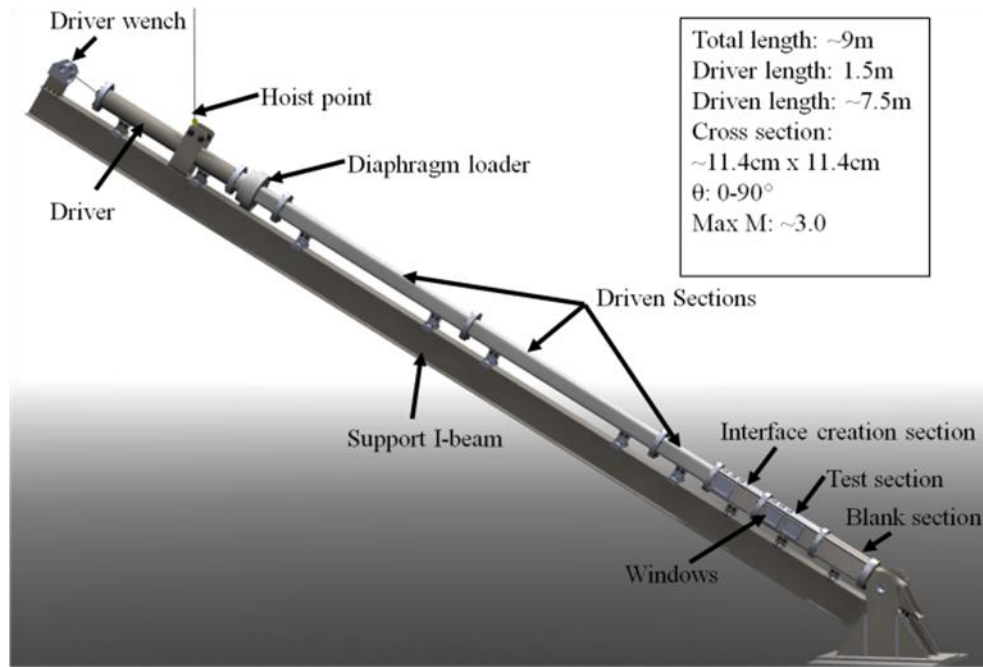
Figure 1: Schematic of the Texas A&M University Shock Tube Facility. [40]

2.1 Facility Sections

The driver is the high-pressure volume that holds the gas that is released to create

the shock wave when the diaphragm located at the bottom of the driver is broken.   The

driver length and pressure restrictions of the design allow for a maximum Mach number

of 2.5 into atmospheric air. Following the driver section is the hydraulic diaphragm

loader that was donated to the TAMU advanced fluid mixing lab by the Wisconsin

Shock Tube Laboratory (WiSTL) at the University of Wisconsin-Madison and was last

used by the Sturtevant group at Cal Tech. This portion of the shock tube is invaluable to

the ability to perform a multitude of experiments in a timely manner. The components

of the diaphragm loader are shown in Figure 2. The diaphragm loader is made up of two

annular pieces that are held together by a steel collar. The annular pieces are then

16

compressed together by two hydraulic rams that can clamp the diaphragm in place with a

force up to 200,000 lbf. A pair of hydraulic return rams is used to reset the position of

the main hydraulic ram of the diaphragm loader. This clamping method allows the shock

tube to be separated and the diaphragm changed without having to remove, replace and

re-torque a bolted connection. The shock tube is separated by a wench that pulls the

driver and the connected portion of the diaphragm loader away from the rest of the

facility. The bottom portion of the diaphragm loader has a sharpened X-shaped blade

that sits slightly below the diaphragm location (Figure 3). The diaphragm comes into

contact with the blade when the pressure difference between the driver and driven

section causes adequate deformation of the diaphragm. This contact causes the

diaphragm to rupture and release the pressure from the driver into the driven section.
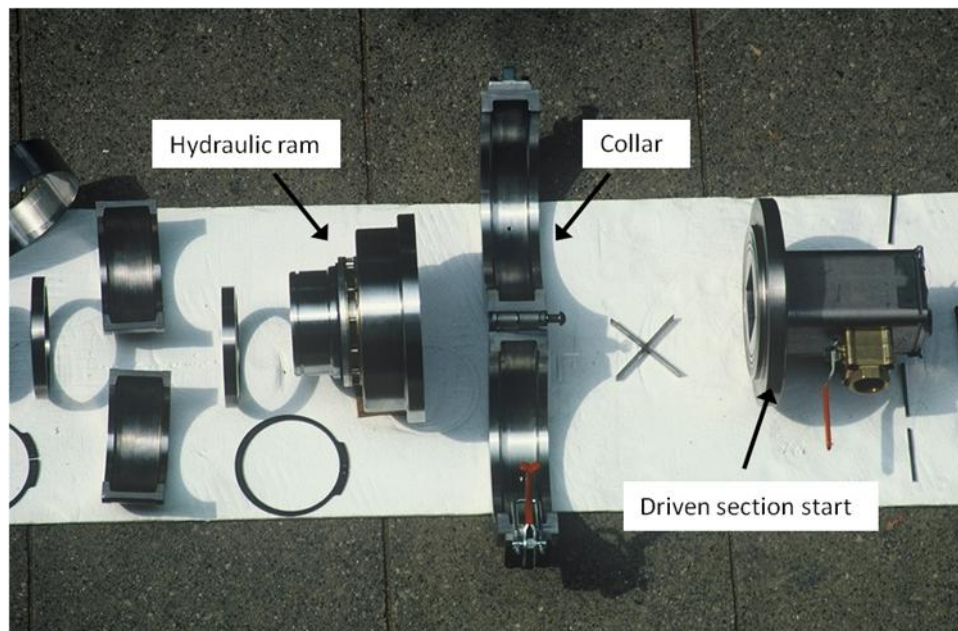
Figure 2: Disassembled diaphragm loader assemebly near its time of initial construction (1980s).

Figure 3: X-blade used for bursting diaphragms.[40]

The driven section of the shock tube was donated along with the diaphragm

loader and shares the same origin. The driven section is made up of three smaller

sections of 4.5 inch square cross-section tube with a combined length of 16ft. The

smaller sections are attached to one another through bolted flange connections similar to

those used to connect the main sections of the facility. The cross-section is not

completely square as the corners have a 3/8" inch fillet which is a byproduct of the tubes

extruded manufacturing. The walls are 0.75 inches thick and the tube is made of

stainless steel. The length of the driven section is necessary to allow for the

compression waves from the diaphragm rupture to coalesce into a planar shock wave.

To allow the facility to reach angles closer to vertical, driven sections can be removed to

alleviate any spatial constraints imposed by the lab space. If sections are removed

calculations must be made to determine if sufficient length remains for the compression

waves to coalesce before interacting with the interface in the test section. The driven

section contains many ports that allow interaction with the inner wall to allow for certain

aspects of the data acquisition systems to be implemented. These ports will be discussed

more in the data acquisition systems section.
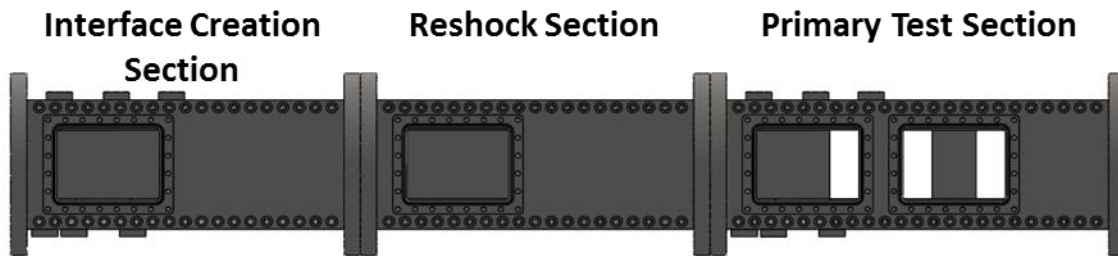
Figure 4: Solidworks model of test section assembly with labeled subsections.

The last section of the shock tube to be discussed is the test section. The test

section is made up of three subsections that are completely modular, shown in Figure 4.

The subsections are a bolted construction with a 4.5 inch cross-section. The subsections

are all different in design and the configuration of the subsections can also be modified

allowing for a wide range of diagnostic systems to be used. The subsections of the test

section are named for their position in the original configuration and help to distinguish

the sections from one another. The interface creation section has interface slots on the

top and bottom to accommodate interface creation inclinations of 30°, 45° and 60° but

can be rearranged to allow for other inclination angles to be used. The front and back

walls of the interface creation section have an opening that can be filled with windows or

aluminum flanges and can be oriented to allow for an exact overlap or no overlap of the

openings. The primary test section, shown in Figure 5, also has the interface creation

slots but is longer in total length than the interface section. The front and back walls of the primary test section have two openings each that can be oriented for exact or staggered overlap. The increased number of openings in the primary test section allows for more data to be collected from that section than the interface section. The third subsection is called the reshock section because it is the section within which the initial shock reflects and interacts. This section is similar in design to the interface creation section except it does not have the interface creation slots on the top and bottom wall.
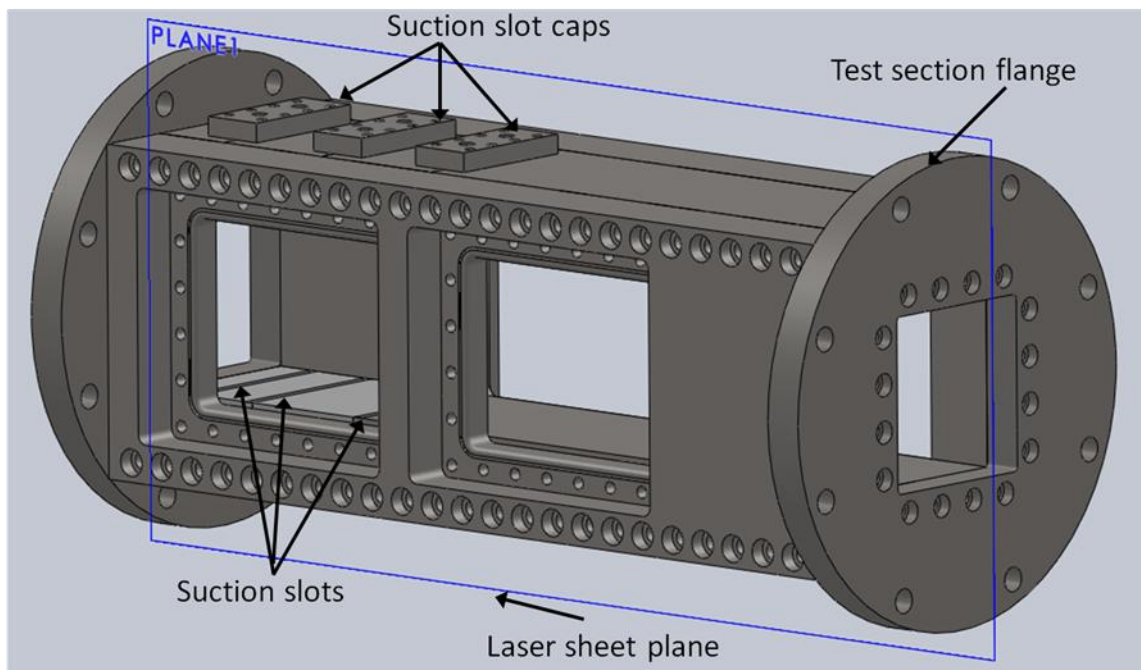
Figure 5: Solidworks model of the primary test section subsection showing the interface creation slot loctations and the laser sheet location noted by the blue plane. [40]

The gas interface in this facility is created by co-flowing light gas from the top of the facility and heavy gas from the bottom of the facility. Valves present at the inlet and interface locations of the facility prevent the high pressure created by the shock wave

from escaping the shock tube. The valves at the interface location allow the gases used to create the interface to vent to the atmosphere to reduce diffusion at the interface and maintain a pressure close to atmospheric pressure.

The interface slots in the test sections are filled with slot fillers to prevent energy loss from the shock wave as it passes the slot openings. The slots that are not being used for interface creation are filled with solid slot fillers that seal the path through the wall at that location. For the slots the gases escape through, a modified slot filler is used to reduce the open area available for the shock wave to travel through while maintaining the ability to allow gas to escape along the entire depth of the shock tube. To prevent seeding particles from being deposited in the small gaps around the slot fillers and the flange connections between the subsections, aluminum tape is applied to the top and bottom walls over the flange and slot filler seams. The tape reduces the amount of trace particles that interfere with our optical diagnostics.

The current windows used in the test section are constructed from acrylic because of the materials similarities and differences to the previous windows that were made of fused silica. The fused silica windows were designed to withstand the high pressures present in the shock tube behind the reshock wave but, due to the material's fragile nature, were housed in a steel frame cushioned by nylon gaskets that acted as a flange to allow for the windows to be bolted into the openings of the test section. Fused silica was chosen for its optical qualities that would allow transmission of the frequencies in the visible spectrum, necessary for the Mie scattering technique, and in the ultraviolet range, necessary for acetone fluorescence in the planar laser induce

fluorescence (PLIF) technique. The window assembly, like the test section, is a bolted

construction designed to allow for full visualization of the tube interior from bottom wall

to top wall. Due to structural stability constraints, a window that would span the entire

length of a test subsection was not possible. In order to achieve the visualization that

was desired, the windows were designed to be six inches in length so that the windows

could be overlapped for extended views while not being so long that they would fail due

to pressure stress. The widow overlap can be seen in Figure 6.
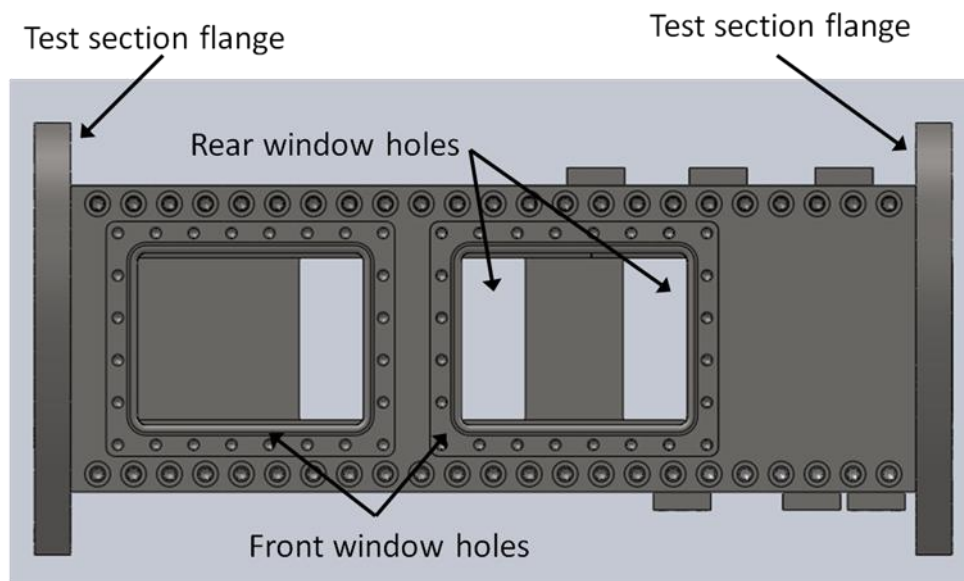
**Figure 6: Solidworks model of the primary test section illustrating the overlapping
visualization areas. [40]**

In an effort to reduce replacement costs in the case of a broken fused silica

window, acrylic windows were designed. The acrylic window design maintains the

strength of the fused silica with a reduced production cost. Another advantage of acrylic

over fused silica is that while fused silica is brittle, acrylic will elastically deform before

catastrophic failure which allows for easier wear detection to predict failure. The downside of the acrylic window is that they have very poor transmittance below 350 nm. The acetone fluorescence spectrum that would be used for PLIF is between 400 and 550 nm. Another issue is that acrylic is highly susceptible to damage from being in the presence of acetone, though acetone vapor does not cause the same level of damage as being in contact with liquid acetone. As an added layer of protection, a thin coating of low density polyethylene (LDPE) is applied to the window. Since the exposure time to acetone vapor is small and cyclic in nature, the windows can be expected to be in use for a significant amount of time. The acrylic windows do not use the same metal shell design that was implemented with the fused silica windows. The acrylic windows are sandwiched between large nylon gaskets with the bolts penetrating through the window itself. To spread the load evenly from the bolts, a steel flange is added to the window assembly (Figure 7).
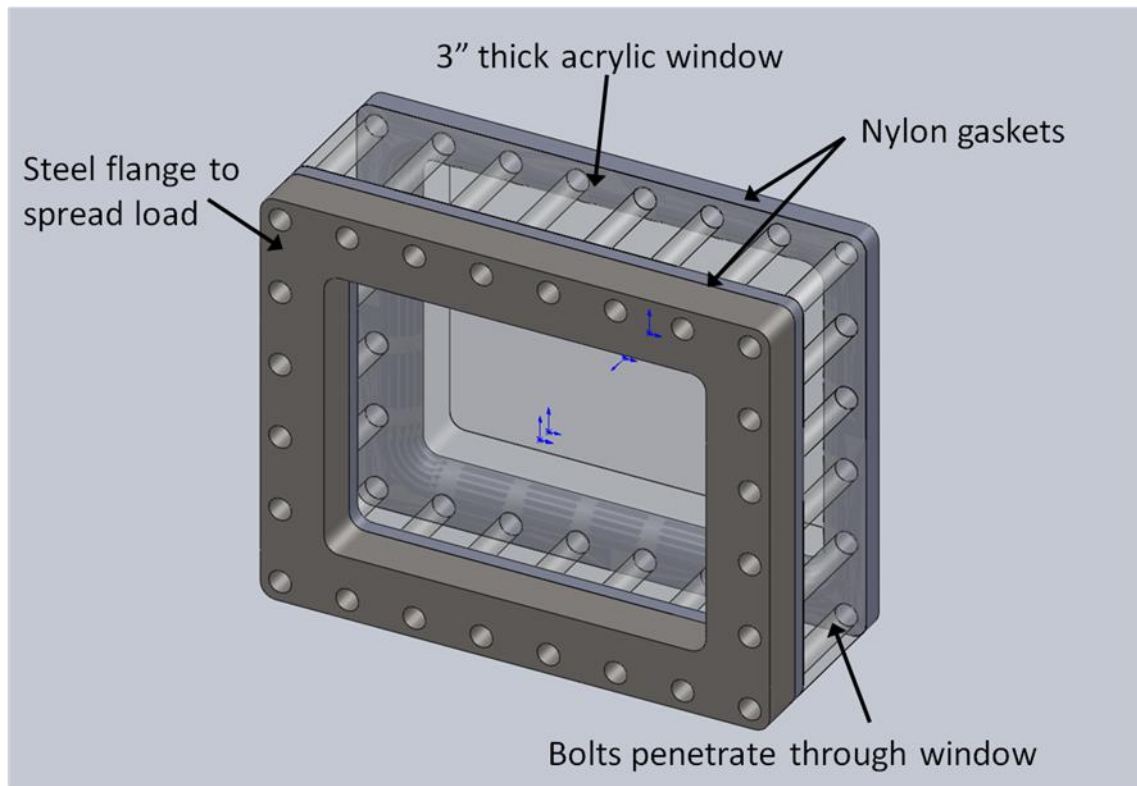
Figure 7: Solidworks model of the acrylic window assembly. [40]

Another window in use in the shock tube facility is located in the flange that acts at the bottom wall of the test section. This window, shown in , allows optical access to the laser sheet necessary for the visual diagnostic systems. This window is made of fused silica for its transmission characteristics and because it has the strength to withstand the substantial pressure placed on it by the reshock wave. The window dimensions were constrained by the transmittance desired and the pressure that the window needed to withstand. If the window was too thin it would fail under the pressure but if it was too thick the laser light would not be able to be effective transmitted.
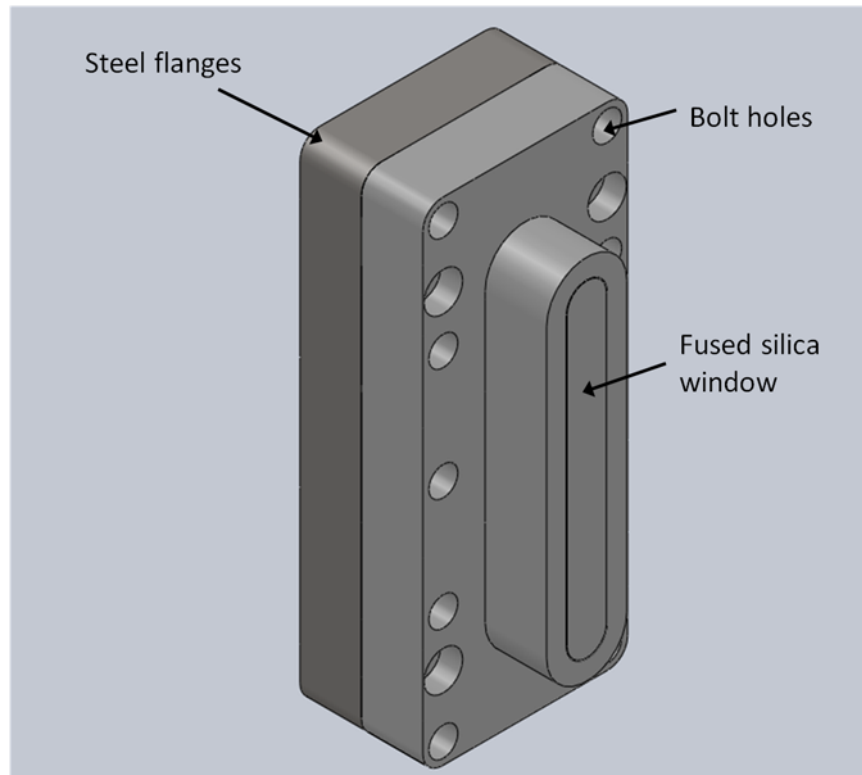
**Figure 8: Solidworks model of laser window in the bottom flange of the shock tube.
[40]**

2.2 Data Acquisition Systems

The data acquisition systems of the shock tube are controlled by a LABVIEW

program running with a 6368 multifunction DAQ. The DAQ supports analog and digital

input and output with the ability to sample at a rate of two million samples per second

per channel. The system has four 32 bit counter timers that allow for precision control

of the valves and cameras up to a rate of 100MHz. The system reads static pressure

from locations in the driver and driven sections as well as in the boost tank that is used

to increase driver pressure to the point of diaphragm rupture. In addition to the static

pressure transducers, four thermocouples are used to obtain temperature measurements

of the initial conditions of the set up. The LABVIEW program also takes readings from 5 dynamic pressure transducers which read at the maximum data acquisition rate. The program has the capability to monitor 8 dynamic pressure transducers (DPT) at maximum data acquisition rate. Two of the dynamic pressure transducers are located in the driven section and are used to detect the initial shock wave and record the speed of the shock before it passes into the test section. Once the shock has entered into the test sections, two more dynamic pressure transducers can record transmitted shock pressure and speed as well as reshock pressure and speed after the shock is reflected. These secondary pressure transducers are mounted into a blank flange that is installed into one of the window locations in the test section. The final pressure transducer is located on the bottom wall of the shock tube and can be used with one of the secondary pressure transducers to determine shock speed as well as recording the maximum pressure reached during the shock reflection. The driven section DPTs detection of the shock wave triggers the counter timers for the laser and camera systems. The delay to the first image and coinciding laser pulse is input into the front panel of the LABVIEW program. The shock wave signal is then sent to TSI Inc.'s Insight 4G which communicates to the first camera connected to capture an image. Insight 4G also communicates with a laser synchronizer that coordinates the laser pulses to fire in conjunction with the cameras' image captures.

The PIV laser system in place on the shock tube utilizes two TSI Inc. Powerview 1.4 MP cameras that have short frame straddling time designed for PIV imaging. These cameras are capable of taking images in very quick succession for PIV measurements.

The shutters of the cameras remain open only when the experiment is in process and the CCD is on for milliseconds but turns off between laser pulses to capture the two images. The timing between the two PIV images is controlled by Insight 4G. The laser used for PIV applications is a dual cavity New Wave Research Gemini PIV laser with the capability of providing 200mJ per pulse at the 532nm wave length that is desired for the chosen tracer particles. The tracer particles are provided by a Peasoup fog machine and the particles are 0.2-0.3 μm glycerine fog. The machine uses high pressure inert gas to pump the particles into the flow.

A sled-and-rail system is used to ensure repeatability in camera position when the area of focus changes from window to window (Figure 9). The rail system is run along the front and back side of the facility and there are multiple sleds to allow for images to be taken at multiple locations. The sleds allow the camera to be attached parallel to the facility and window face and aimed at a large adjustable mirror to allow the window to be in the cameras field of view. After calibrating the focus and correctly framing the image, the camera position on the sled is locked into place. The sled can then be moved from testing location to testing location and the camera will be in correct position. A feeler arm is used to ensure that the sled position relative to the window is consistent each time the sled is moved.
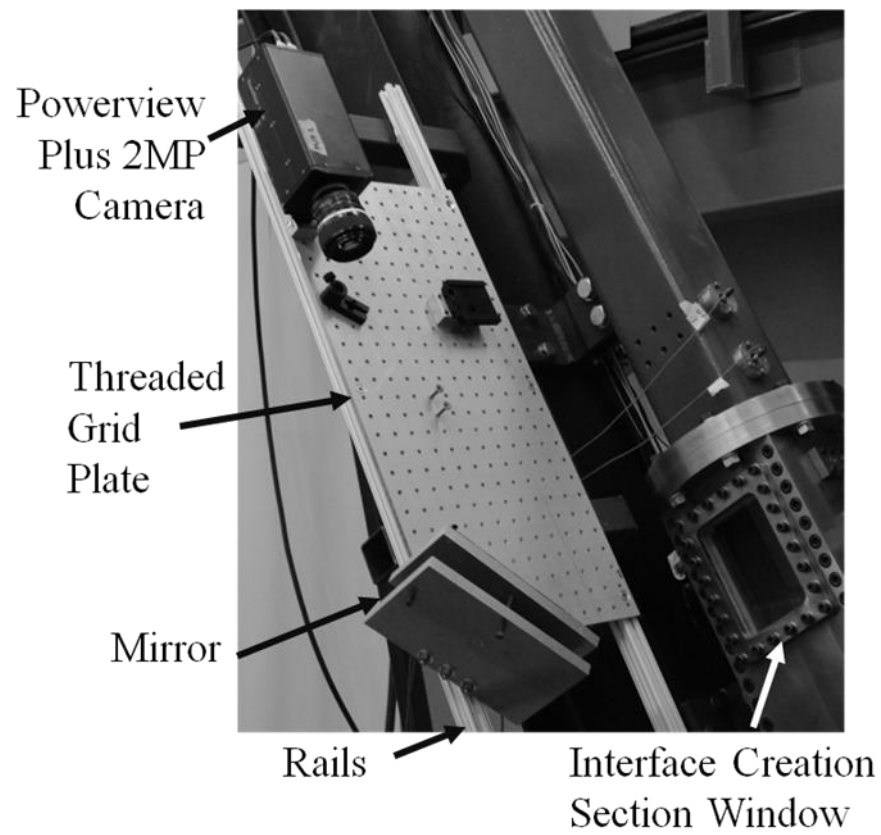
Figure 9: Sled-and-rail camera mounting system. [40]

3. EXPERIMENTAL SETUP

This section will present the standard experimental method used and define the experimental cases for all the work presented herein. The differences in procedure to accomplish the different data acquisition methods are discussed in the experimental method subsection. After discussing the experimental method, the method of choosing the experimental cases and their defining characteristics are presented to provide an introduction to the experimental work that will be presented in a later section.

3.1 Experimental Method

The experiments presented in herein were performed with a N_2 over CO_2 interface ($A \sim 0.23$) at a facility inclination angle of $60°$. The gas pair was chosen based on the moderate Atwood number and their availability from the supplier. The inclination angle was set using an overhead crane that raised the facility to the correct inclination allowing a tube steel stand to be put into position to hold the facilities weight. The stand is then bolted to anchors sunken into the lab floor to assist in carrying the static load from the facility. A digital inclinometer is used to ensure the angle desired is achieved to an accuracy of $\pm 0.05°$. The shock strength for all experiments was Mach 1.55 and was achieved by breaking a 0.030" thick polycarbonate diaphragm.

In order to ensure accurate visual results, before the tube is filled the cameras and lasers are calibrated for the imaging location of interest. A calibration block is used at the imaging location that allows for the lasers and camera to be calibrated simultaneously. The calibration block has a photo and ruler on the side that is oriented toward the camera that assists in focusing the camera on the center plane of the test

29

section. After the camera is focused, an image is taken of the calibration block that is used to quantify the millimeters per pixel of the experimental images taken at that location. The downstream side of the calibration block has a series of dots scribed into the surface to allow both a beam and a laser sheet to be aimed into position down the center plane of the shock tube.   Once the cameras and laser system is properly aligned, the tube is filled with seeded gas and images are taken of the interface to check image quality and seed density.

The Mie scattering technique visualization technique was used in this work to capture the fluid interface development as well as for acquiring the PIV image sets. For the qualitative interface images, the light gas was heavily seeded with fog particles created by the fog machine discussed in the data acquisition systems section. The fog is mixed with pure N_2 in a fog mixing chamber which provides a large mixing volume (~8 ft^3) compared to the volume within the shock tube. The mixed fog and nitrogen are injected into the tube through a port, controlled by a solenoid valve, in the driven section prior to the test section. The fog density and other gas flow rates into the facility are controlled by mass flow controllers. To control the fog density, qualitative measurements are made using an LED and photodiode oriented opposite of one another at the exit of the fog mixing chamber. The voltage read from the photodiode is inversely proportional to the amount of fog that is entering the facility and is used to determine if the seeding level of the gas entering the tube is at the desired level. The N_2 and CO_2 flowrates (~5 L/min and 3 L/min respectively) are monitored to achieve a balanced interface. Once the interface is stabilized and the fog solenoid valve is opened, the light

gas flow rate is shut off to allow the seeded gas to fill the entire light gas portion of the shock tube. The tube is allowed to fill for approximately 20-30 minutes to allow the seeded gas to fill the light gas portion before the experiment is performed.

As the incident shock travels though the driven section, the speed of the wave and the pressure rise across the wave are recorded by the dynamic pressure transducers in the driven section prior to the test section. The speed of the wave is determined by taking the distance between the transducers and dividing that by the difference in pressure rise time of the two transducers. Pressure measurements from the other dynamic pressure transducers in the facility can be similarly used to determine the speed of the transmitted, reflected and other secondary waves created by the incident shock's interaction with surfaces in the facility. The pressure rise recorded by the driven section DPTs is used to trigger the counters in the LabVIEW program that control the timing of the lasers and cameras that are used for data acquisition.

The method for capturing PIV images is similar to that for the qualitative image series with small alterations. The light gas is seeded using the same system but the seeding density is much less than what is desired for the qualitative images. For PIV images, the heavy gas is also seeded using a small canister containing dense fog from the fog machine. A small amount of fog is added to the heavy gas to match the light gas seeding. The seed density must be sparse enough that individual particles can be observed in the images. The time between images for the PIV measurements is determined by comparing the resolution of the processing and the bulk fluid velocity. Using the calibration determine mm per pixel, the image resolution can be converted

from pixels to mm and the time for the particles to move the resolution distance can be calculated. This is the time used for the delay between the PIV images. Insight 4G observes the motion of particle patterns and creates vectors to show the movement in the flow field. Using the calibration and the time between images, the movement is converted into distances traveled in the x-direction and y-direction as well as velocities in the same directions. The vectors created from this information are exported from Insight 4G to be processed.

After each experiment is performed, a blank flange is removed from each part of the test section to vent the tube to atmospheric pressure and allow the operators access to clean the test section to remove any residue from the seeding particles. The windows are cleaned to remove any fog residue that could obscure the field of view. Data from the images and the pressure transducers are inspected after each run as a check that the tube is functioning properly before the next experiment is performed.

3.2 Experimental Case Definition

The three experimental cases presented in this work are a product of creating the interface in different locations within the test section and the desire to have the greatest imaging ability possible when the reshock interaction occurs. These factors dictated that the primary test section of the test section would always be the against the bottom wall of the shock tube. The orientation of the other subsections of the test section would be determined by the desired interface creation location. The interface creation section was the only remaining subsection that was designed to create an interface so its location was the primary factor in the test section orientations for each case. The test section

orientations for each experimental case are depicted below in Figure 10:Solidworks model of the test section configurations for Case 1 (A), Case 2 (B) and Case 3 (C).Figure 10.
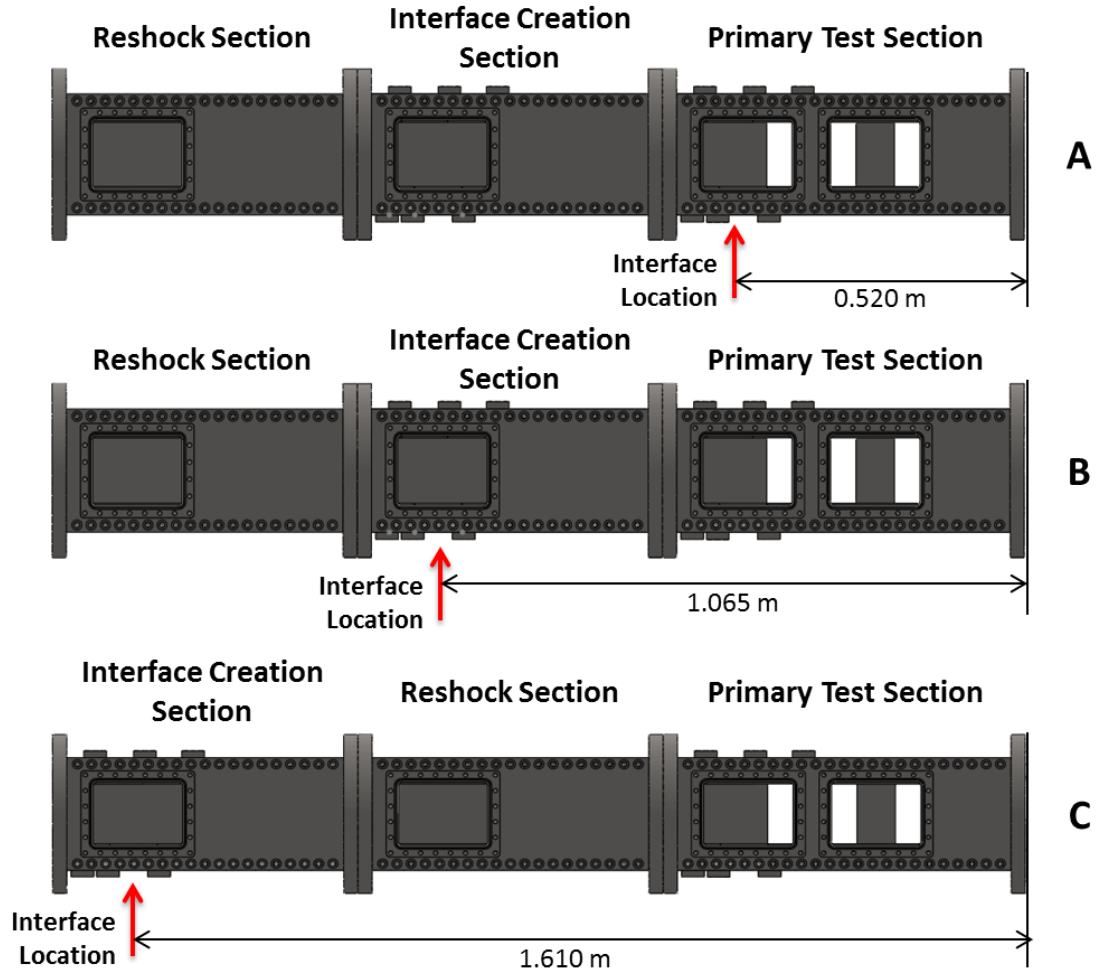
Figure 10:Solidworks model of the test section configurations for Case 1 (A), Case 2 (B) and Case 3 (C).

The three experimental cases are distinguished from one another by their initial interface location and development time but share common fundamental aspects. All experimental cases presented have the same facility inclination angle, θ, of 60°, gas pair

of N_2 over CO_2, which corresponds to an Atwood number of $A \cong 0.23$, and incident

Mach number of $M = 1.55$. By sharing the same inclination angle, the cases share the

same amplitude-to-wavelength ratio, $\eta/\lambda = 0.29$.

The importance of creating the initial interface in different locations is to allow

the initial RMI to develop for different amounts of time. The different levels of

development provide different interface conditions for the reshock to interact with in the

primary test section. The different interface development times before reshock are

proportional to the development times after reshock before the expansion waves begin to

effect the RMI development. Estimated development times for each case and location of

the shock wave during the experiment are shown in the x-t plots for Case 1, 2 and 3 that

are shown in Figure 11, Figure 12 and Figure 13 respectively. From these plots, the

imaging location and the time period that the reshock development can be studied can be

calculated as well as determining the location within the facility where the reshock

interaction will occur. Once this location is determined, the appropriate window

location in the primary test section is chosen and the camera set up for each experimental

case can be determined.
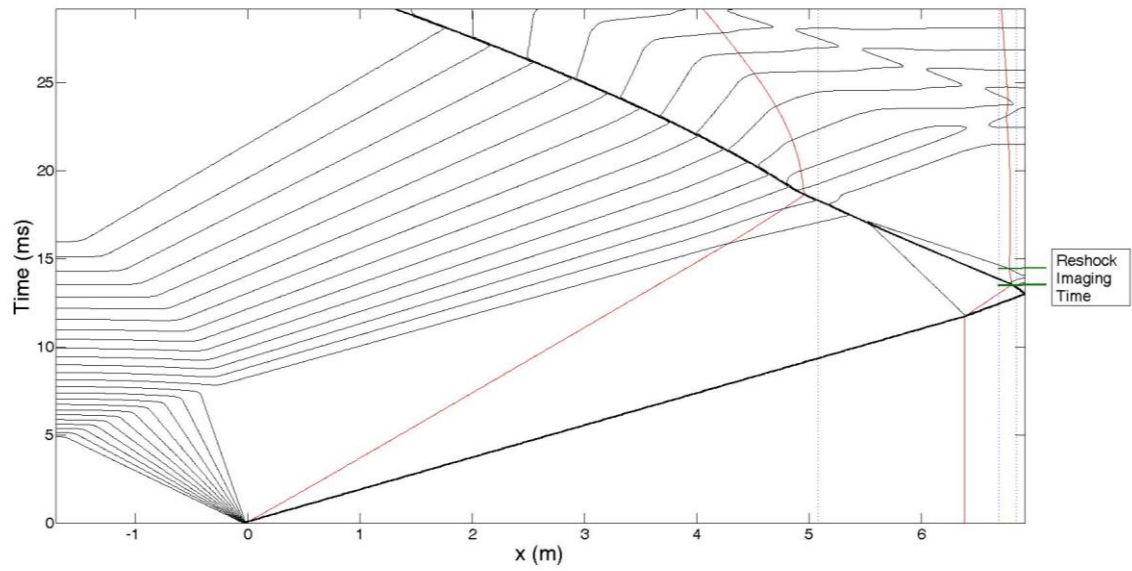
Figure 11: Case 1 x-t plot with reshock imaging time
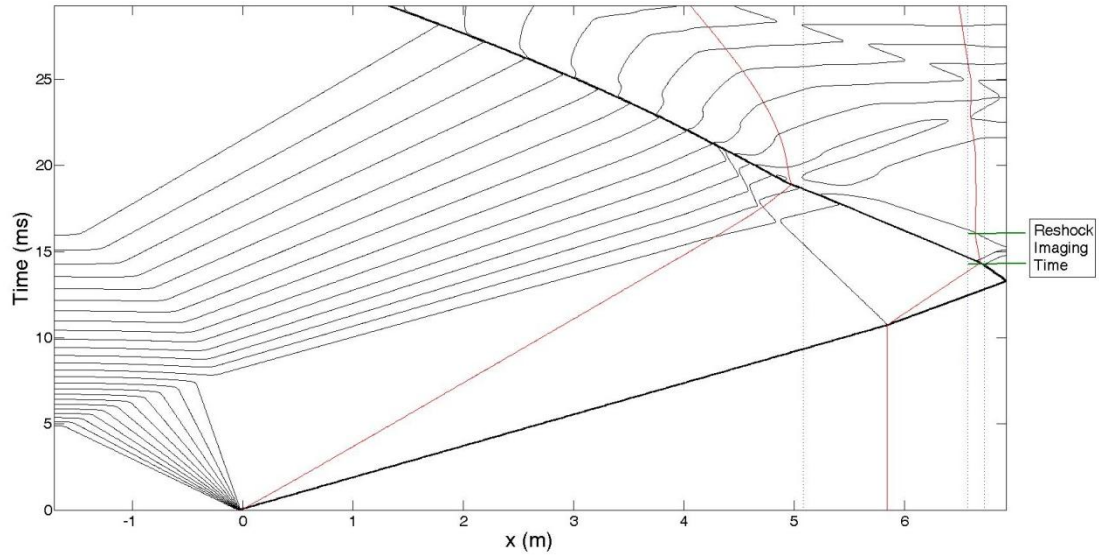
Figure 12: Case 2 x-t plot with reshock imaging time

35
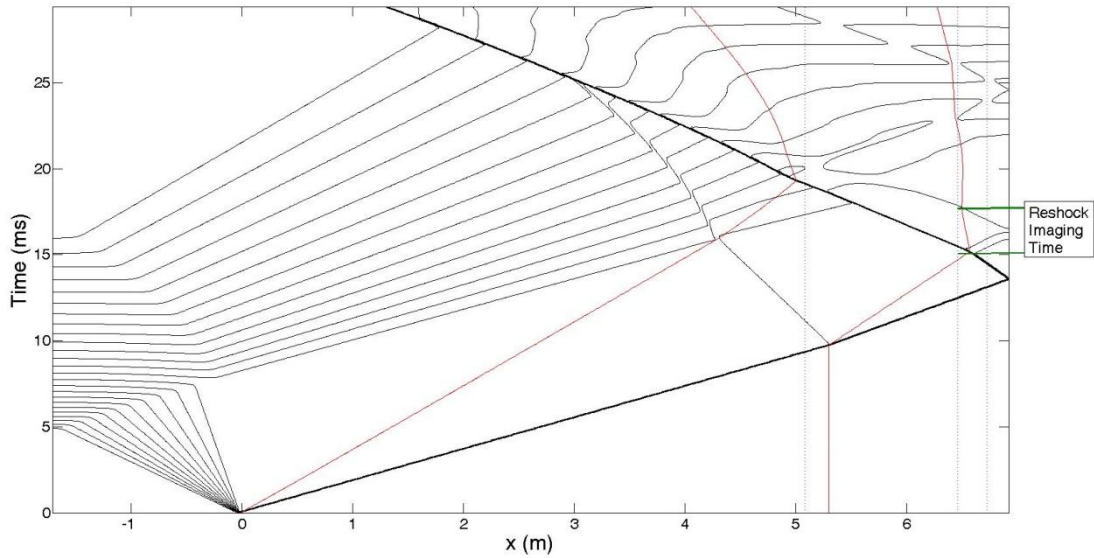
Figure 13: Case 3 x-t plot with reshock imaging time

The initial shock development times for each of the cases lead to different levels of development of the interface with a longer development time relating to a more complex interface. For Case 1, the interface has approximately 1.635 ms to develop from the initial shock interaction before the reshock wave interacts with it and a reshock development time of 0.921 ms before the expansion waves begin to effect the RMI development. The Case 2 initial interface is created almost twice the distance from the bottom wall as Case 1 and similarly has almost twice the development time, approximately 3.50 ms as well as an increased reshock development time of 1.681 ms. Case 3's interface is created the farthest from the bottom wall of the shock tube and predictably has the most development time from the initial and reshock interactions at approximately 5.105 ms and 2.571 ms respectively. The pre-reshock interfaces for the three experimental cases are all stages of development of the initial condition for the

36

facility settings described. The development of the pre-reshock interfaces are shown in Figure 14 below.
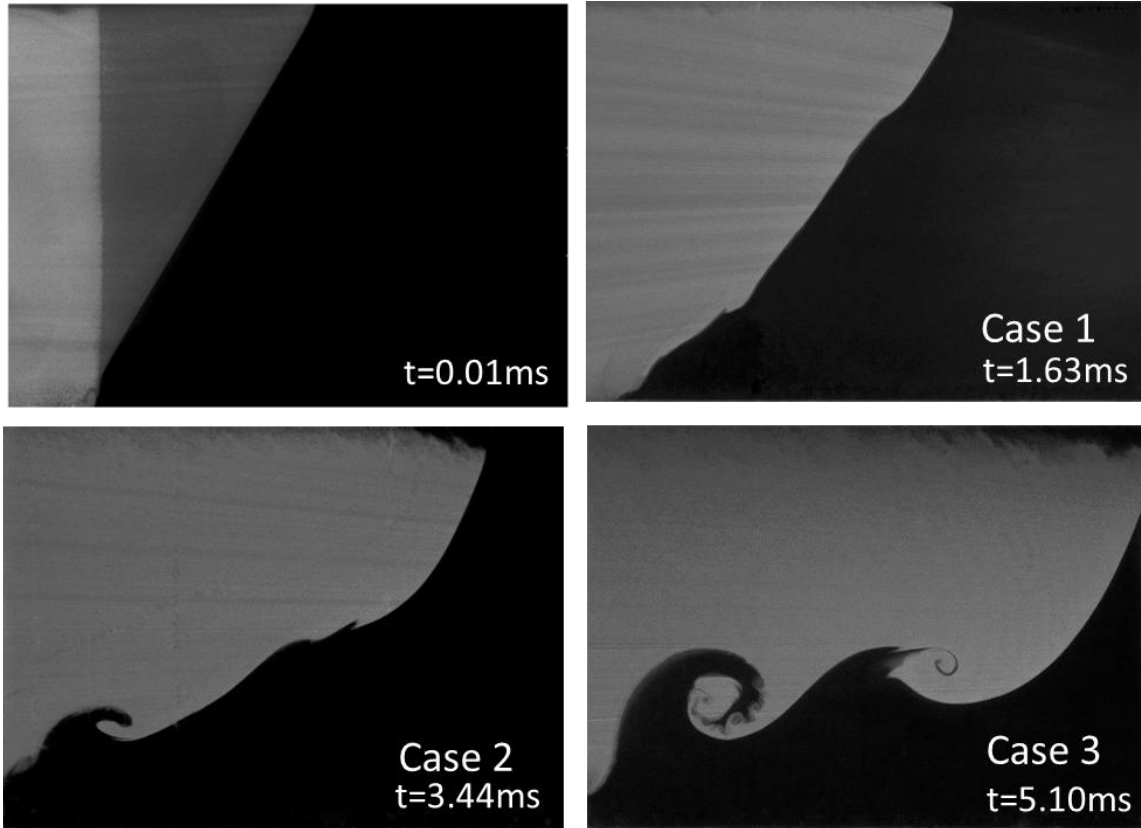
Figure 14: The pre-reshock interface conditions for Cases 1, 2 and 3 with the initial conditions shown for reference. Times are in relation to instant of interaction of initial shock and initial interface.

The pre-reshock interface of Case 1 is similar to the common initial conditions for the three cases but contains many inflection points. Along with the inflection points, the beginnings of what could develop into vortical structures can be seen as sharp points on the interface from the heavy gas into the light gas. The pre-reshock conditions for Case 2 show that the inflection points visible in Case 1's pre-reshock interface have begun to develop into more well-defined vortex structures as evidenced by the small

primary vortex on the trailing edge of the interface. Other inflections present in the Case 1 interface have begun to cause heavy gas protrusions into the light gas. The interface has also stretched during the development between the two cases causing the difference between the initial interface angle and the developed interface angle to increase. Case 3 presents the most developed pre-reshock interface of the three experimental cases. The primary vortex structure that was not very developed in the Case 2 pre-reshock interface has now grown and become more developed. There is also evidence of shear driven Kelvin-Helmholtz instabilities present in the interface in the primary vortex structure. The heavy gas protrusion present in the Case 2 pre-reshock interface has traveled further into the light gas and is beginning to roll up near the tip of the protrusion. The protrusion also appears to be part of a larger secondary vortex structure that is beginning to develop. A matrix detailing the important parameters defining the experimental cases is shown in Table 1 below as a summary.

Table 1: Defining parameters of experimental cases.

	Case 1	Case 2	Case 3
Angle	60°	60°	60°
a/λ	~0.29	~0.29	~0.29
Atwood Number	~0.23	~0.23	~0.23
Mach Number	1.55	1.55	1.55
Initial interface distance from bottom wall	0.520 m	1.065 m	1.610 m
Approximate initial shock development time	1.635 ms	3.50 ms	5.105 ms
Approximate reshock development time	0.921 ms	1.681 ms	2.571 ms

4. EXPERIMENTAL RESULTS

The results of the performed experimental work will be presented in this section. A qualitative analysis of the results will be presented first in the form of image series detailing the development of the interface. After the qualitative examination, the interface will be studied quantitatively through measurements of mixing width, interface length and velocity. The velocity measurements will be used to calculate circulation, enstrophy and turbulent kinetic energy spectra.

4.1 Qualitative Results

A high temporal resolution series of Mie scattering images detailing the development of the post reshock interface in each of the three experimental cases has been acquired. To create the desired contrast between the two gases composing the fluid interface, the light gas (N_2) was seeded with glycerin fog particles using the method described in section 3.1 to cause it to fluoresce to appear bright in the images. The heavy gas (CO_2) was left unseeded and thus appears black in the images. The images were processed to remove background noise and seam lines along the opposite wall of the facility. Also, the region of unseeded CO_2 was identified using a threshold and its brightness was reduced to increase the contrast between the two gases in the images. All images for Cases 1 and 2 were taken using a single imaging window. The growth of the interface after reshock in Case 3 necessitated imaging using overlapping window locations simultaneously to have sufficient viewing area. An image series of the interface development from the initial shock is provided in Figure 15 for comparison.
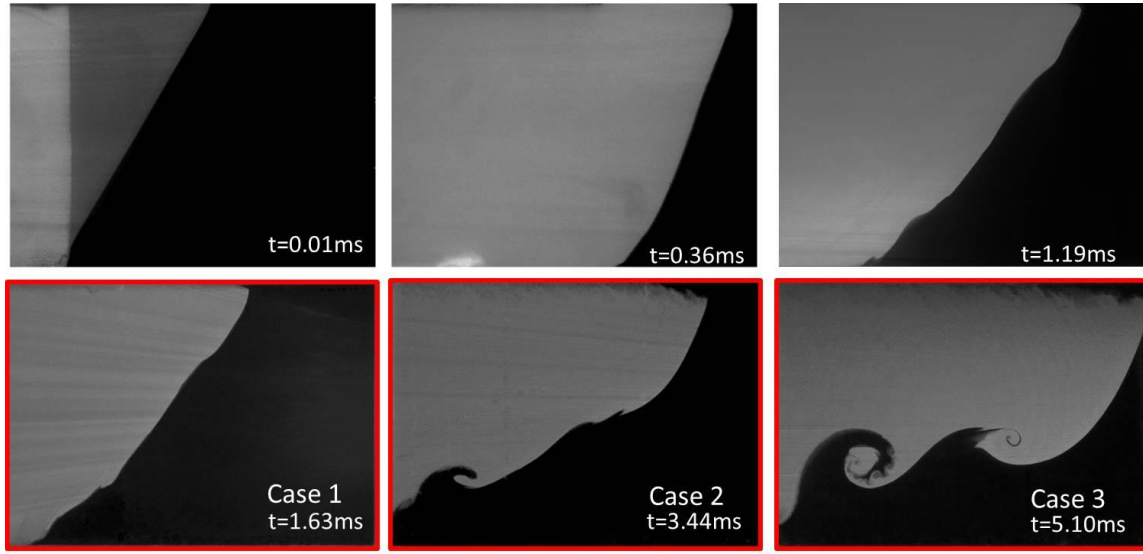
Figure 15: Interface development from the initial shock interaction.

The first time series of Mie scattering images, shown in Figure 16, are for the development of Case 1 after reshock. As previously discussed, the interface pre-reshock has no well-defined vortex structures, only the inflections that would become the structures if allowed further development. The inflections are annotated to correspond to the vortex structures that will be present in the more defined cases for comparison. These inflection points stretch and rotate clockwise while the interface rotates counter-clockwise. The bright area in the image at $t_r = 0.04$ ms is the reshocked light gas that appears brighter due to the compression of the reshock wave. The gradient between the reshocked light gas and other light gas is the reshock wave that is curved, rather than planar, because of the difference in acoustic impedance of the two gases. Since the heavy gas has a higher acoustic impedence, the reshock wave travels slower through it than through the light gas causing the the shock to bend because of the difference in speed. First appearing in the image at $t_r = 0.24$ ms, a dark triangle begins to form in the

bottom left hand corner of the images persisting to $t_r = 0.84$ ms and beyond. The

boundary of the triangular region is a slip line that will be discussed in more detail in the

quantitative results section. Also of note, there is a halo effect on the light gas side of

the reshocked interface that is most visible at later times. The author believes that this is

a product of a refractive index mismatch between the gases.
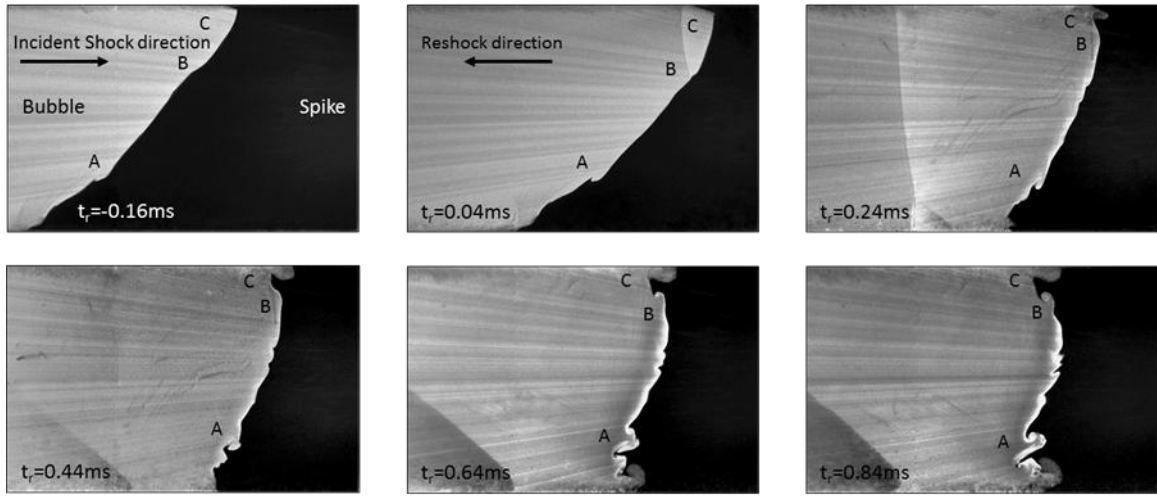
Figure 16: Case 1 Mie scattering image time series. Times are relative to reshock interaction time.

In the image series for Case 2, shown in Figure 17, inflection point A from Case

1 has developed into the primary vortex structure which is crushed when the reshock

wave interacts with it. The inflection point at point B is stretched and grows into a small

protrusion into the light gas. The interface edge at point C also turns into another spike

as the interface rotates counter-clockwise. Once the rotation has stopped, the structures

created by the reshock's interaction with the vortex structure and the interface inflection

points continue to advance into the light gas as small-scale structures develop. Similar

to Case 1, the reshock wave bends because of the gas property differences and causes a

42

slip line to form in the bottom left hand corner. In the post-reshock interface for Case 2, the structures are well distributed along the interface and the structure size is larger than the main vortex structure that was present in the pre-reshock interface.
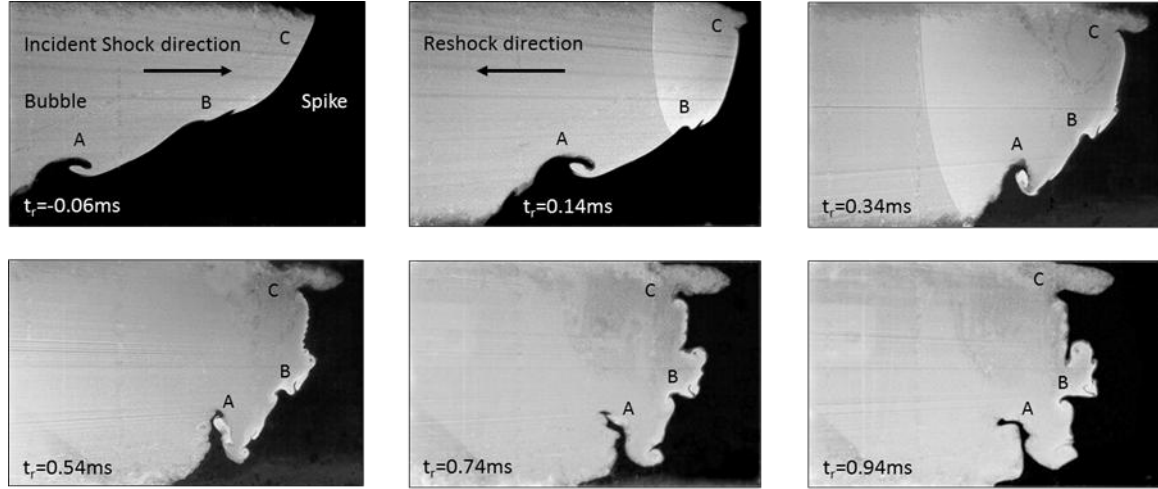
Figure 17: Case 2 Mie scattering image time series. Times are relative to reshock interaction time.

The final series of Mie scattering presented is for the most developed case, Case 3. The pre-reshock interface has two well-developed vortex structures with Kelvin-Helmholtz vortex structures present in the primary vortex due to high shear and vortex-accelerated RTI-like growth. The pre-reshock structures are large and are well distributed along the interface. The large structures begin to compress before the reshock has passed completely through the interface, as shown in the $t_r = 0.13$ ms image of Figure 18. After the reshock wave has fully progressed through the interface the large structures have been crushed and are no longer distinguishable while the bubble tip, annotated as point C, protrudes into the light gas similar to Case 1 and 2. Along the top wall of the shock tube near point C there is a region of brighter fog that is caused by fog

deposition in the seams in the top wall being entrained into the flow. A similar effect
has been observed previously along the bottom wall and a similar solution will be
implemented to reduce the effect. Though not as visible as in Case 1 and 2, the slip line
from the previous cases is still present.
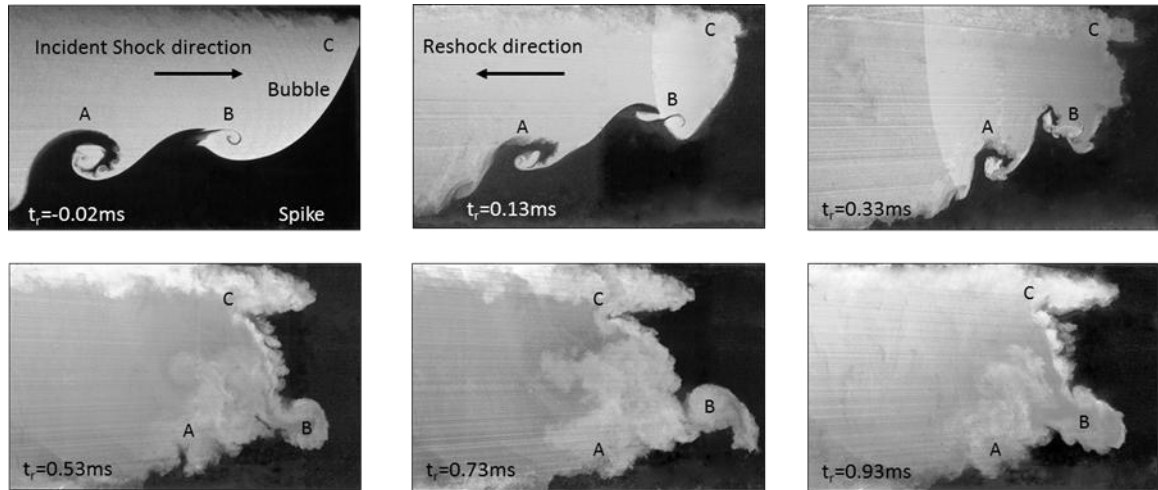
Figure 18: Case 3 Mie scattering image time series. Times are relative to reshock interaction time.

4.2 Quantitative Results

The initial quantitative data presented in this section will be mixing width and interface length measurements taken from the Mie scattering images presented in section 4.1. These measures can be used to calculate interface growth rates to describe the behavior of the interface during its development. These growth rates can be used to calculate the Reynolds number of the flow field which can then be used to calculate the length scales associated with the flows, shown in section 4.2.3.

The quantitative data presented in sections 4.2.2 – 4.2.4 uses vector sets created by Insight 4G's processing can be used to take a more detailed look at the interactions that are present in the flow field before and after the reshock interaction with the interface. Glycerin fog particles were used as tracers in the flow and were introduced using the method described in section 3.1. The time between images used for the PIV technique was selected using the resolution of the camera and the flow velocity at the time of interest. The resolution was determined to be four pixels, which is approximately 0.457 mm using the calibration of 0.1143 mm per pixel that was determined from the calibration image. With the flow velocity of the pre-reshock flow determined to be approximately 250 m/s, the delay time between the images was calculated to be 5μs. Similarly, the post-reshock flow velocity was determined to be approximately 40 m/s which yields a delay time of approximately 25 μs. By tracking particle patterns from image to image to determine distance and specifying the time between images, particle velocities can be calculated and plotted as a vector field. Insight 4G creates the vectors using a recursive Nyquist grid with a minimum spot size

of 8-by-8 pixels, fast Fourier transform (FFT) correlation and a Gaussian mask with a signal-to-noise pass ratio of 1.5. The minimum spot size used to velocity vectors determines the resolution of the measurements, preventing the author from collecting data at every point in the flow field. Instead data is collected on a grid with spacing half that of the minimum spot size. This grid spacing can sharpen gradients between data locations that would be seen as smooth at higher resolution.

The simulations were performed by Jacob McFarland for the author using the ARES code used in his previous works [17], [40], [61], [62]. The ARES code is classified as an Arbitrary Lagrange Eulerian (ALE) code. ALE codes utilize an Eulerian grid that is allowed to move during a Lagrangian time step after which the nodes can be remapped to the Eulerian grid after the time step. ALE codes also have the ability to be used as a purely Eulerian or Lagrangian code. Eulerian codes have trouble tracking interface locations but are effective for modeling fluid flows. Lagrangian codes can faithfully track interfaces but must be remapped to allow nodes to concentrate in areas of high density. ALE codes allow for a single code to model fluid flows with interfaces and maintain the strength of both Eulerian and Lagrangian codes.

4.2.1 Mixing Width and Interface Length
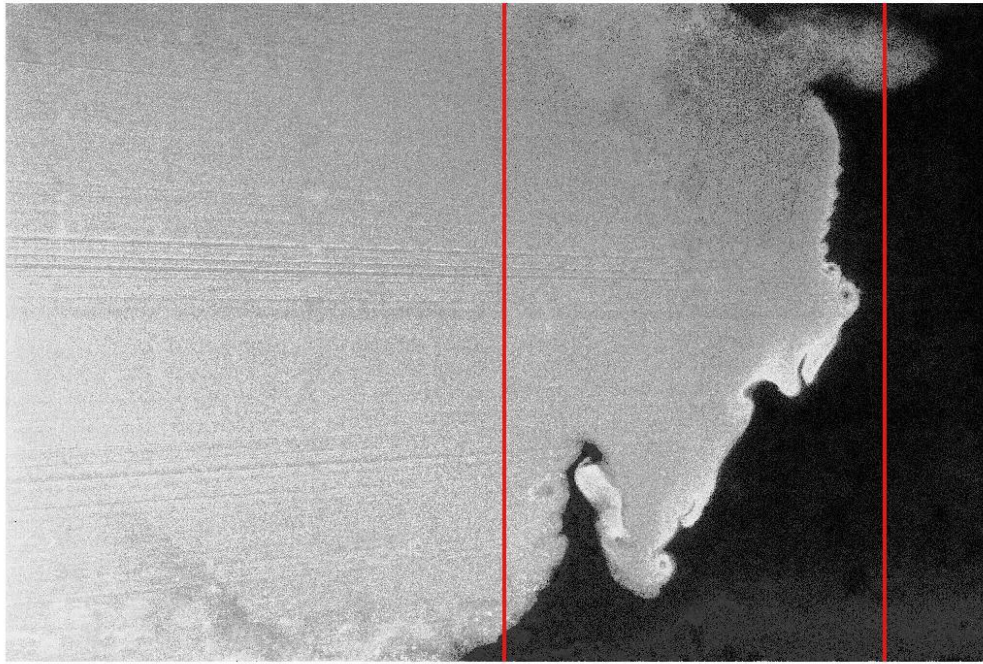
Figure 19: Case 2 post-reshock image with mixing width annotated.

The Mie scattering images can provide an estimation of the mixing that is

happening at the interface by calculating the mixing width. To calculate the mixing

width, the image is converted into a binary image by using an intensity threshold. Once

the image is purely black and white, the columns of pixels where the image is 5% and

95% white are determined working from the left and right edges of the images inward

and the pixel distance between the columns is recorded. The pixel distance is converted

into a distance by using the calibration image. The mixing width measurements for the

images in the three experimental cases are presented with data from the initial shock

development for reference in Figure 20.
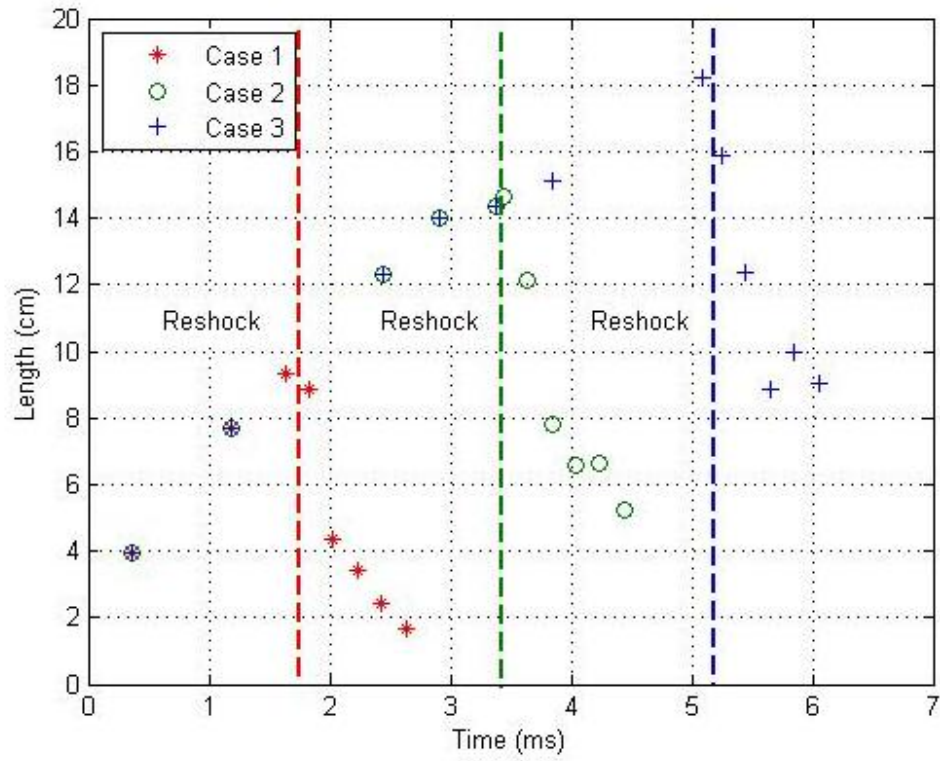
Figure 20: Experimental mixing width for Cases 1, 2 and 3.

The mixing width for each of the cases is compared to simulation results in Figure 21. Even though the flow field becomes increasingly three-dimensional after reshock, the experimental mixing width data still shows good agreement with the simulations. The mixing width data can be used to calculate the interface growth rate for all three experimental cases.
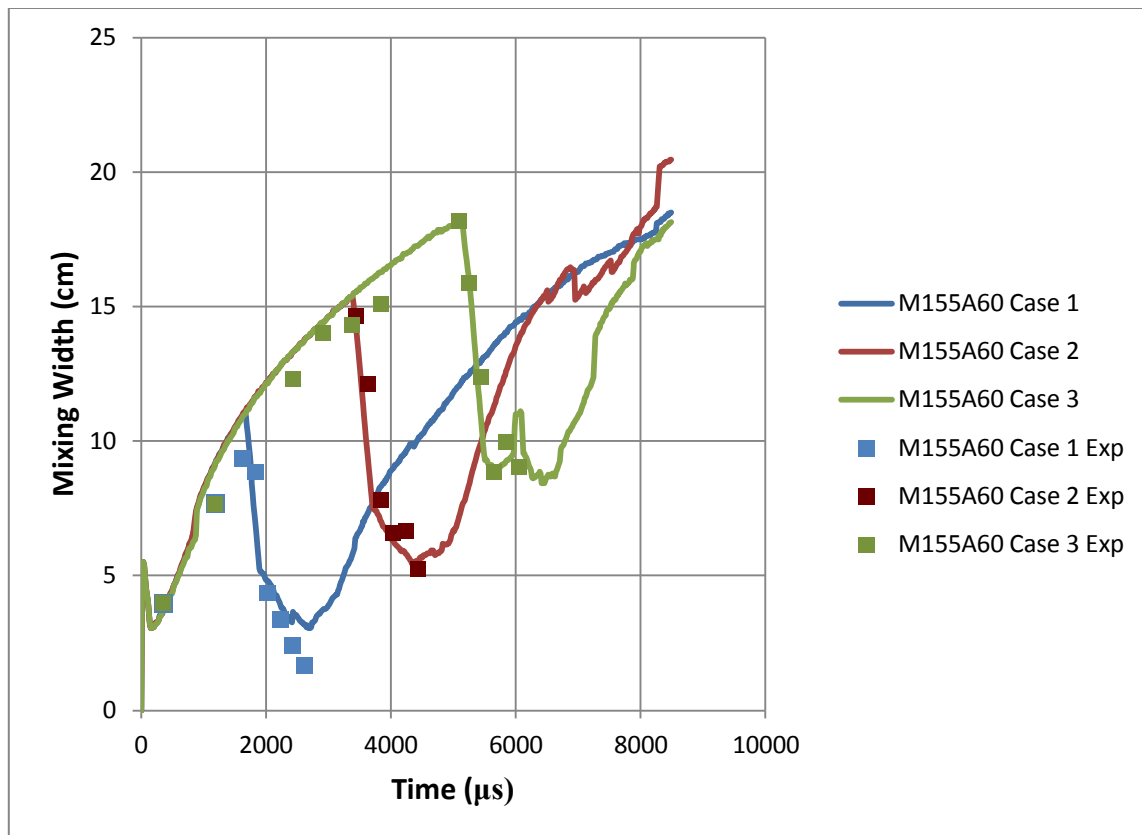
Figure 21: Comparison of experimental and simulation calculated mixing width.
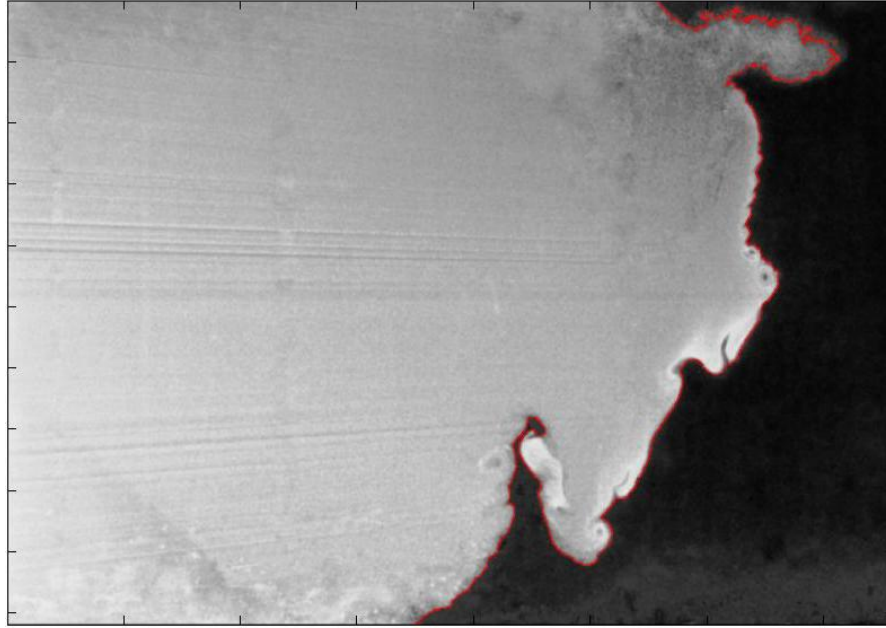
Figure 22: Case 2 post-reshock image with interface length annotated.

The Mie scattering images can also be used to measure the length of the interface as it stretches. To measure the interface length, the image is filtered to reduce noisy gradients then the image was analyzed by rows of pixels to find the sharpest gradient within a 1 pixel range of the previous point. The pixel length is then converted to a distance in cm using the calibration image. The interface length for all three cases is shown in Figure 23. The interface length for Cases 1 and 2 are shown to continue growing after the reshock interaction while Case 3 appears to shrink after reshock. A study of the Mie scattering images for Case 3, presented in section 4.1, show that the lost interface length can be attributed to the collapse of the large structures present before reshock. The collapse of these structures mixes the formerly defined interface that defined the structure beyond the point where the interface between the gases can be observed. This issue was discussed by Kumar *et al.* [63] who found that once material

begins to be entrained into vortex cores, the interface can no longer be accurately tracked

using the described method since the interface lines could begin to coincide with one

another. This leads the author to believe that the interface length can be used to

faithfully investigate the interface in Cases 1 and 2, but not for Case 3. The interface

length can also be used to compute an interface growth rate.
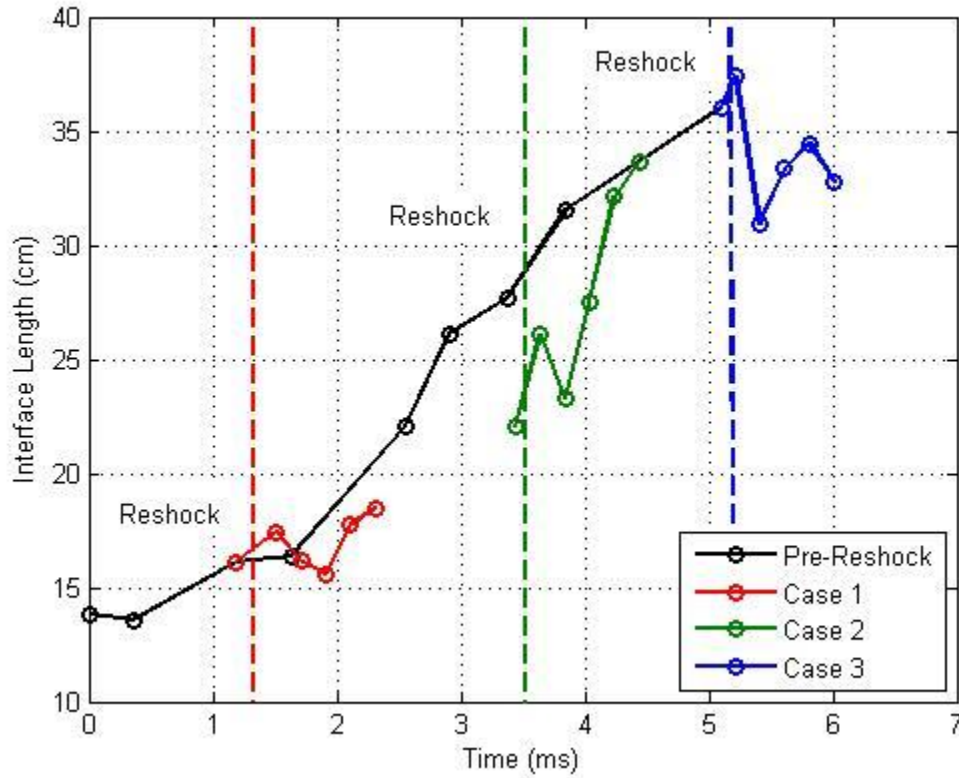
Figure 23: Interface length for all three experimental cases.

The interface growth rates that are calculated using the mixing width and

interface length are shown in Table 2: Interface growth rates based on mixing width and

interface length.Table 2. The pre-reshock growth rates for the mixing width calculation

methods were determined to be the same for the three cases which is expected as all

three experimental cases derive their pre-reshock conditions from the same interface development. The pre-reshock growth rate shows the interface to be stretching at a rate of 29.7 m/s. The post-reshock growth rates for the three cases are slightly different in magnitude but are all found to be around 90 m/s. This result is consistent with the work done by Lienov *et al.* who found that reshock interaction time did not affect the interface growth rate. Similar to the mixing width calculated growth rates, the pre-reshock growth rates for the interface length method was found to be 47.9 m/s for all three cases. The post-reshock growth rates are vastly different due to the different levels of interface development for the pre-reshock condition of each experimental case. The growth rate for Case 2 is drastically larger than that of Case 1, 114.4 m/s and 15.61 m/s respectively, while the growth rate for Case 3 is found to be -33.96 m/s. The growth rates would suggest that post-reshock Case 2 grows more than Case 1, which can be observed in the Mie scattering images. Due to the inability for this method to track the interface faithfully due to the level of development present in Case 3 after reshock, the interface length growth rate for this case after reshock cannot be deemed valid for comparison.

The growth rates computed from the mixing width and interface length can be used to determine the Reynolds number of the flow using equation (4.5),

$$\mathrm{Re} = \frac{\delta \dot{h}}{\nu} \tag{4.5}$$

where δ is the mixing width (interface length), $\dot{h}$ is the mixing width (interface length) growth rate, and ν is the kinematic viscosity.

Table 2: Interface growth rates based on mixing width and interface length.

	Case	Mixing Width Growth Rate (m/s)	Interface Length Growth Rate (m/s)
1	Pre-reshock	29.7	47.9
	Post-reshock	-83.76	15.61
2	Pre-reshock	29.7	47.9
	Post-reshock	-92.27	114.4
3	Pre-reshock	29.7	47.9
	Post-reshock	-97.75	-33.96

4.2.2 Vorticity, Circulation and Enstrophy

The vorticity of the flow field was calculated from the curl of the 2D velocity field for all three experimental cases. Due to the gradient nature of vorticity, eq. (4.1), the calculated numerical derivatives produced a noisy vector field. The boundary layer created by the shock tube walls was found to have vorticity that interfered with the mapping of the flow field vorticity and therefore was cropped from the data set to avoid this interference.

$$\vec{\omega} = \vec{\nabla} \times \vec{u} \qquad (4.1)$$

In an effort to obtain more accurate derivatives, empty spaces in the vector fields were filled using a median of the nearby values and then the field was smoothed using a median filter with a bin size of 11-by-11 pixels.

The vorticity plot and corresponding Mie scattering image for Case 1 pre-reshock is shown in part A and B of Figure 24. As previously discussed the interface has no defined vortex structures, only inflection points. The vorticity plot for this time of Case 1 supports this observation by defining the interface as a line of diffuse negative vorticity with regions of stronger vorticity corresponding to the inflection points of the interface. After the reshock interaction, the interface is shown as a diffuse line of positive vorticity with regions of strong vorticity that correspond to the structures on the interface that were inflection points prior to reshock. The vorticity at the interface is reversed due to the application of baroclinic torque and the inflections present before reshock begin to manifest themselves as small structures that can be seen in both the vorticity plot and its corresponding Mie scattering image, shown in parts C and D of Figure 24.
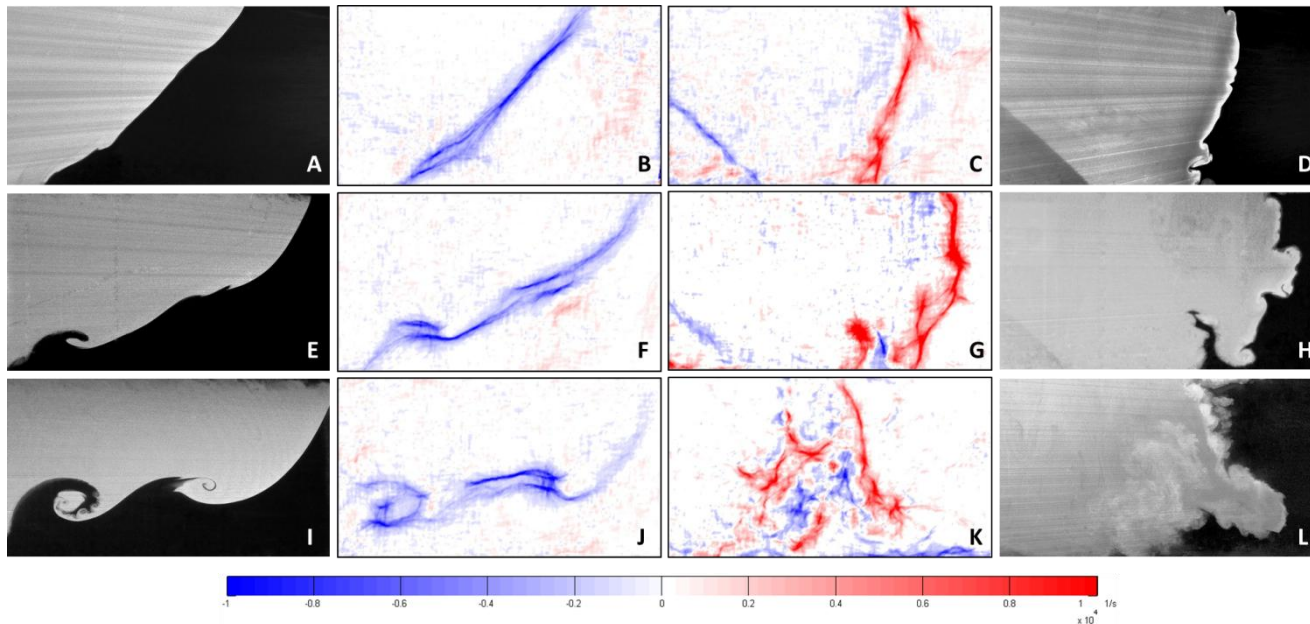
Figure 24: Mie scattering and vorticity plots for Case 1 before (A, B) and after (C, D) reshock, Case 2 before (E, F) and after (G, H) reshock and Case 3 before (I, J) and after (K, L) reshock.

The slip line visible in the Mie scattering images is visible as a line of negative vorticity post-reshock. This will be discussed in detail after Cases 2 and 3 are presented.

The pre-reshock vorticity plot for Case 2, part F of Figure 24, shows the small vortex structure that is starting to form near the trailing edge of the interface as well as the small protrusion that is starting to extend from the interface, both features are also present in the corresponding Mie scattering image, part E of Figure 24. Similar to the structure that is shown in the Mie scatterig image, the areas of strong vorticitywithin the diffuse vorticity of the interface correspond to the vortex structure and inflection points. After the reshock interaction, the second application of baroclinic torque again reverses the direction of the vorticity of the interface except for a small portion where the applied torque acts with the pre-reshock negative vorticity allowing it to remain. This pocket of negative vorticity corresponds to the structure that was a defined vortex structure prior to reshock. The line of negative vorticity marking the location of the slip line is again present in this case.

Case 3, shown in part I-L of Figure 24, is the most developed pre-reshock interface and as such has larger regions of stong vorticity within the diffuse representation of the interface. After the second application of baroclinic torque, the large structures are crushed beyond visible recognition in the Mie scattering images, the remnants ot the vorticity of the structures are still visible after reshock. Large areas of both negative and positive vorticity are present supporting the mixing that is seen in the Mie scattering images and are also similar to the effect of vortex collapse seen in Case 2.

The thin line of negative vorticity that is present in the bottom left corner of the post-reshock images is a lambda shock leg that is created by the incidence angle of the reshock and the wall. As the reshock travels through the interface, a portion of the wave is reflected as a curved shock that travels towards the bottom wall where it reflects again and interacts with the transmitted shock. The interaction between the bottom wall reflection and the transmitted wave creates a triple point. As this triple point travels up the facility, it leaves a lambda shock leg behind it marking its path that serves as a boundary for the dark region of the Mie scattering images and creates the line of negative vorticity in the post-reshock vorticity plots. On the upstream side of the lambda shock, the flow accelerates in order to return the reshock wave to a planar state. A pseudocolor plot of the streamwise velocity is presented in Figure 25 to illustrate the velocity jump across the lambda shock. The slip line has been measured to be approximately 60° which is a product of the Mach reflection interaction with our inclined interface of approximately the same angle. The velocity difference across the lambda shock causes shear along it and determines the direction of the vorticity of the slip line. If allowed more time to develop, Kelvin-Helmholtz vortex structures could develop along the slip line, but the structure would likely be below our visible

resolution.
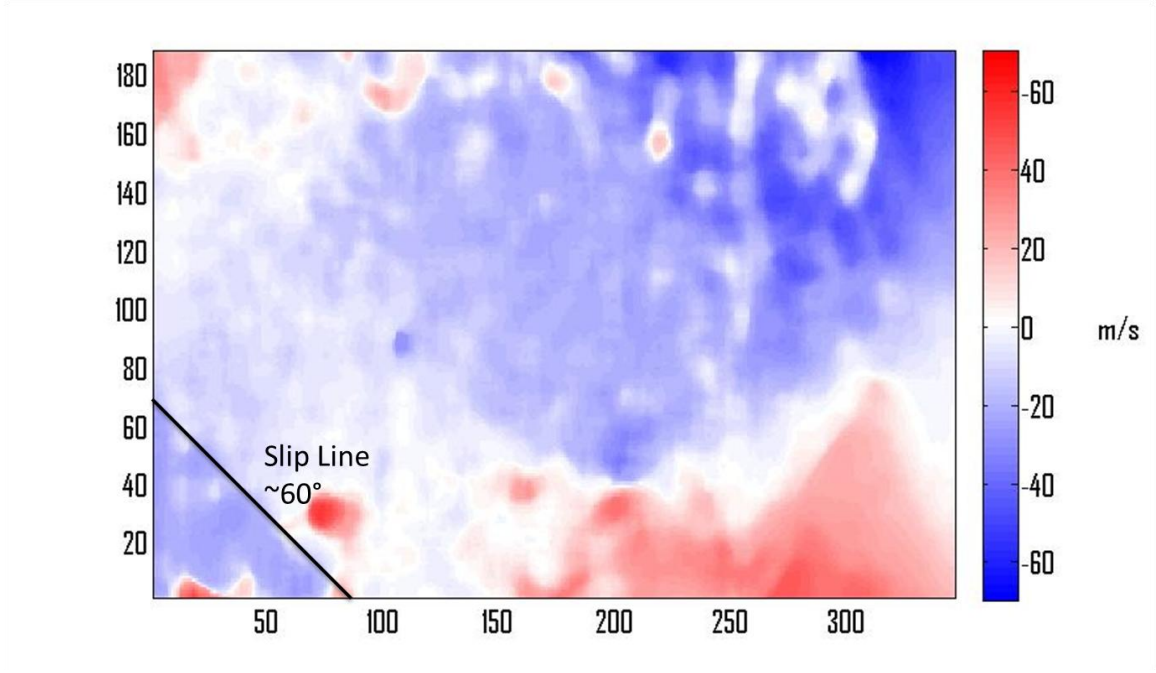
Figure 25: Case 2 psuedocolor plot of streamwise velocity

The vorticity data collected for multiple runs at the same image time for each case before and after reshock was integrated over the flow field to determine the ensemble average circulation and enstrophy present, shown in . The equations for enstrophy and circulation are provided, in equation (4.2) and (4.3) respectively, where Γ is circulation, ε is enstrophy, $\vec{\omega}$ is vorticity, and $d\vec{S}$ is a differential area element.

$$\Gamma = \iint_S \vec{\omega} \cdot d\vec{S} \tag{4.2}$$

$$\varepsilon = \tfrac{1}{2} \int_S \vec{\omega}^2 \, d\vec{S} \tag{4.3}$$

Enstrophy is related to the kinetic energy of the flow that corresponds to dissipation effects in the fluid. It is a better representation for this than circulation which sums both positive and negative vorticity which can lead areas of high vorticity to cancel out obscuring the level of activity in the flow. The enstrophy across the reshock interaction for all cases increases which shows that there is more local rotation occurring in the post-reshock flow fields. As the large, coherent structures of the interface break down during the post-reshock development and smaller scale structures are developed, the rotational motion of the flow is enhanced locally as it is dissipated from the larger scales. Case 1 possesses fewer coherent structures than the other cases post-reshock and therefore, its post-reshock enstrophy is found to be less than that of Cases 2 and 3. Case 2 is found to have more post-reshock enstrophy than Case 3, however. This could be caused by resolution limitations on the PIV measurements preventing smaller scales from being included in the enstrophy calculations.

Circulation provides an overall description of the fluid rotation in the flow field at a given time and location. The circulation ensemble averages are compared to the standard deviation of the same experiments to obtain a standard error to obtain a measure of repeatability. With coefficients of variance less that 7%, the pre-reshock portion of Case 1 and the pre- and post-reshock values for Cases 2 and 3 are seen to be repeatable, while the variation of the post-reshock circulation for Case 1 is larger but well within the range of experimental error.

Table 3: Circulation and Enstrophy Stastics

Case	Before or After Reshock	Number of Experiments	Ensemble Average Enstrophy $(m/s)^2$	Ensemble Average Circulation (m^2/s)	Standard Deviation	Cofficient of Variance
1	Before	10	2.10E-04	-4.117	0.285	6.93%
	After	11	3.20E-04	4.540	0.822	18.10%
2	Before	9	6.53E-04	-5.073	0.297	5.86%
	After	14	5.13E-02	7.333	0.430	5.86%
3	Before	14	1.39E-04	-4.889	0.277	5.67%
	After	9	1.26E-02	7.884	0.319	4.04%

The experimental data for enstrophy and circulation is compared to simulation results in Figure 26 and Figure 27, respectively. The experimental values of enstrophy do not agree with the simulation predicted values, falling well short of the predicted magnitude. In the simulations, the enstrophy peaks immediately after reshock and then declines quickly. The experimental enstrophy for Case 1 does not reach the level of the simulations post-reshock but this could be because the experimental interface's simplicity does not generate as much enstrophy or than the simplicity causes the level of enstrophy to decline at a quicker rate. In Case 2, the experimental enstrophy does not agree with the growth of enstrophy predicted leading up to the reshock interaction time and over predicts the level on enstrophy after reshock. The enstrophy of Case 3 experimentally is much less than the simulation values.

The ensemble average values of the total circulation for all 3 cases pre- and post-reshock show good agreement with the simulations, however the positive and negative circulation components do not agree with the simulations. For Case1, the pre-reshock circulation values, positive, negative and total, are all in agreement with the simulation values. This can be a product of the simplicity of the pre-reshock interface. Post-reshock for Case 1 shows a good agreement between the experimental and simulation total circulation, but the positive and negative components are not in good agreement with the simulations. The circulation values for Case 2 are again found to be in good agreement with the simulations for the total circulation values but experimentally are less than the simulation value for the circulation components. The same trend is seen in the Case 3 circulation data as well. The difference in experimental and simulation values can be partially explained by the method used to calculate the experimental circulation. The presence of numerical gradients in the more complex post-complex interface would produce coupled positive and negative vorticity around the gradient, which when totaled would cancel out leading to good agreement with the simulations on the total circulation. It is likely that the binning and filtering processes implemented in the vector creation and vorticity calculation could lead to resolution differences that would prevent the experimental results from capturing smaller scales that would add to the positive and negative components of the circulation.

61

The magnitudes of the circulation in the three cases before reshock interaction are similar and, as expected, the less-developed Case 1 possesses less circulation than the other two more-developed cases. The post reshock circulation values follow a trend that themore development time allowed prior to reshock interaction, the larger the change in circulation and magnitude of post-reshock circulation. This supports the idea that increased development of the pre-reshock interface leads to a more complex interaction between the interface and the reshock wave which causes more circulation to be present in the flow field. The Reynolds number of the flow field based on circulation can be calculated using equation (4.4)

$$\mathrm{Re} = \frac{\Gamma}{\nu} \qquad (4.4)$$

.
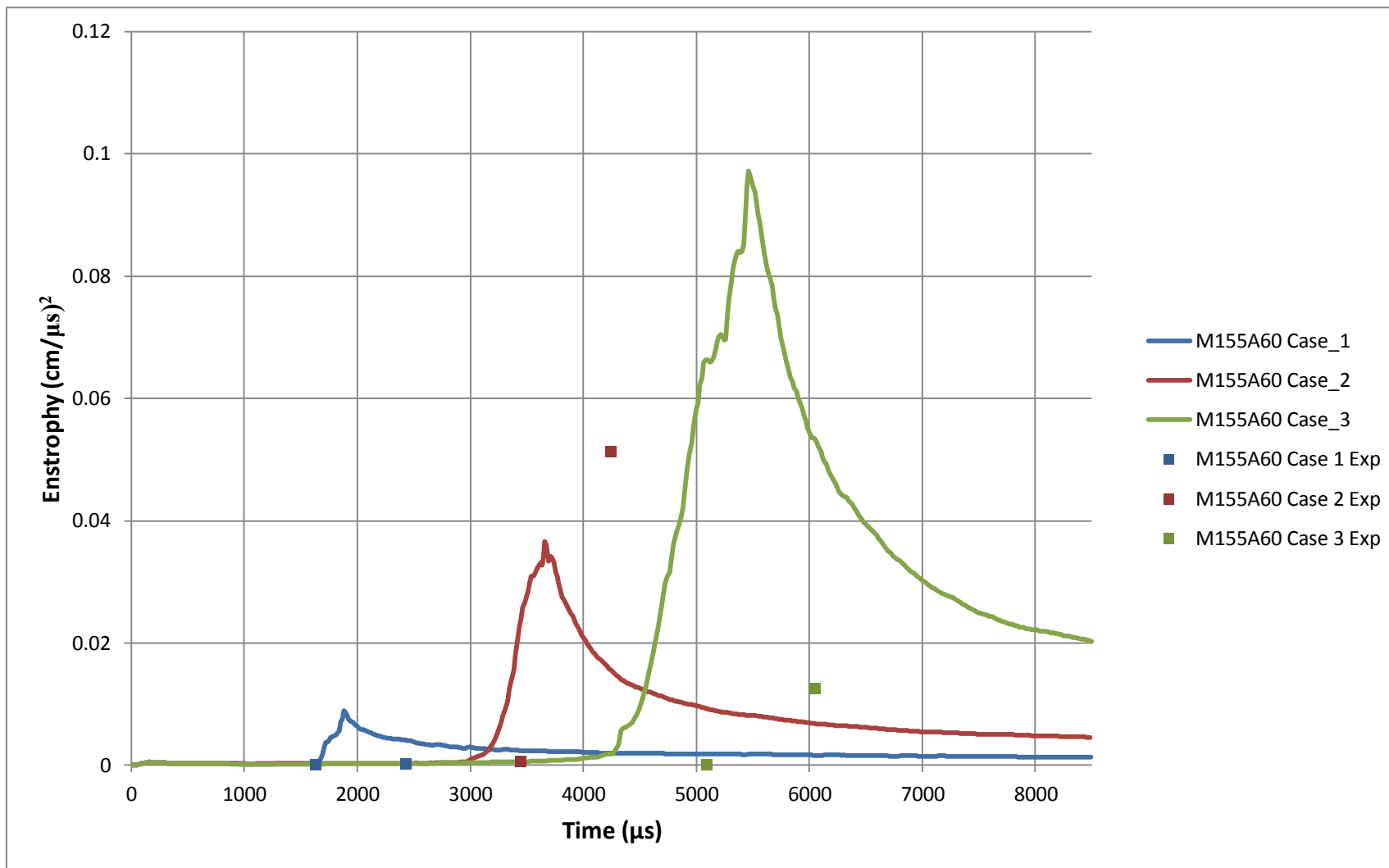
Figure 26: Experimental and simulation calculated enstrophy
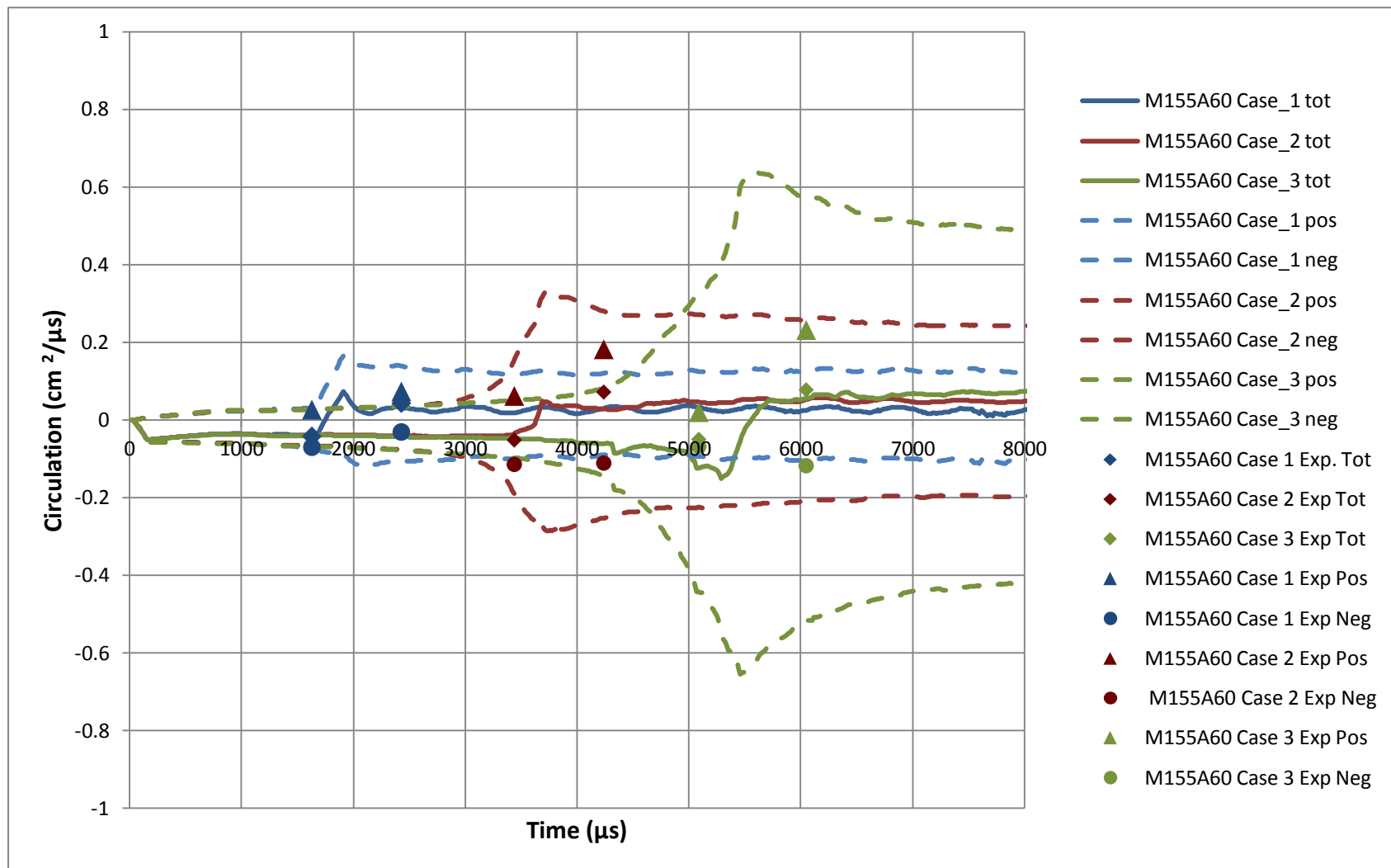
Figure 27: Experimental and simulation calculated circulation.

4.2.3 Turbulent Length Scales

From the Reynolds number, the turbulent length scales of the flow can be calculated. These Reynolds numbers along with the one calculated from the circulation can be used to determine the turbulent length scales of the flow. The length scales of interest to the author are the Kolmogorov length scale and the Taylor microscale. The Kolmogorov length scale corresponds to the scale at which viscosity begins to dominate the flow field and dissipate the energy of the flow field into heat. The Taylor microscale is the scale at which viscosity begins to have a profound impact on the dynamics of turbulent eddies in the flow field. The Kolmogorov scale is defined by equation (4.6) and gives an estimate of the high-wave-number end of the inertial subrange.

$$\lambda_k = \delta \operatorname{Re}^{-3/4} \tag{4.6}$$

where λ_k is the Kolmogorov length scale, δ is the largest length scale, and Re is the Reynolds number. The Kolmogorov length scale based on different Re for the three experimental cases is presented in Table 4. The scales for the different Re are between 10^{-7} and 10^{-5} m which is two orders of magnitude below the resolution of the experimental PIV measurements. It can therefore be concluded that the experimental results are unable to capture any mixing taking place at the Kolmogorov scale.

Table 4: Kolmogorov length scales based on different Reynolds numbers.

Case		Re based on mixing width growth rate		Re based on interface length growth rate		Re based on circulation using mixing width as length scale		Re based on circulation using interface length as length scale	
		Re	λ_k (μm)	Re	λ_k (μm)	Re	λ_k (μm)	Re	λ_k (μm)
1	Pre-reshock	576234	4.466	1605000	3.577	855217	6.472	855217	5.736
	Post-reshock	821415	0.880	1132000	5.114	1855000	.478	1855000	3.531
2	Pre-reshock	903218	4.997	2194000	3.867	1054000	4.51	1054000	6.703
	Post-reshock	2488000	1.053	12850000	1.281	2996000	0.916	2996000	3.817
3	Pre-reshock	112300	5.276	3584000	4.372	1016000	2.92	1016000	11.25
	Post-reshock	4959000	1.179	4295000	3.281	3222000	1.629	3222000	4.07

66

The Taylor microscale gives an estimate of the largest scales which are isotropic and independent of large-scale features in the flow field and is defined by equation (4.7).

$$\lambda_L = \delta \, \mathrm{Re}^{-1/2} \tag{4.7}$$

where λ_L is the Taylor microscale and δ is the largest length scale. The Taylor microscale based on the different Re are presented in Table 5. The Taylor microscales are calculated to be 10^{-4} and 10^{-5} which is on the same order as the PIV resolution. Since the Taylor microscale is of similar order of magnitude as the PIV resolution it is plausible that the beginning of the intertial dissipation subrange would be detectable. This conclusion will be investigated in the next section.

Table 5: Taylor microscale based on different Reynolds numbers.

Case		Re based on mixing width growth rate		Re based on interface length growth rate		Re based on circulation using mixing width as length scale		Re based on circulation using interface length as length scale	
		Re	λ_L (μm)	Re	λ_L (μm)	Re	λ_L (μm)	Re	λ_L (μm)
1	Pre-reshock	576234	123	1605000	127.3	855217	196.8	855217	174.4
	Post-reshock	821415	26.48	1132000	166.8	1855000	17.62	1855000	130.3
2	Pre-reshock	903218	154	2194000	148.8	1054000	142.6	1054000	214.8
	Post-reshock	2488000	41.84	12850000	76.69	2996000	38.13	2996000	158.8
3	Pre-reshock	112300	171.8	3584000	190.2	1016000	92.68	1016000	357.3
	Post-reshock	4959000	55.64	4295000	149.3	3222000	69.03	3222000	172.4

4.2.4 Turbulent Kinetic Energy Spectra

Turbulent kinetic energy (TKE) spectra are used to quantify the scales over which energy is distributed. The method used to calculate the spectra presented in this work was similar to the method used by Latini *et al.* [49] with the exception that density weighing was not employed. First, vorticity plots for each case were examined and the boundary layers (clearly visible in the vorticity plot) were cropped. Because only half of a wavelength is studied in the inclined shock tube, as seen in Figure 28, the PIV data was reflected across the bottom, horizontal boundary (the floor of the shock tube).
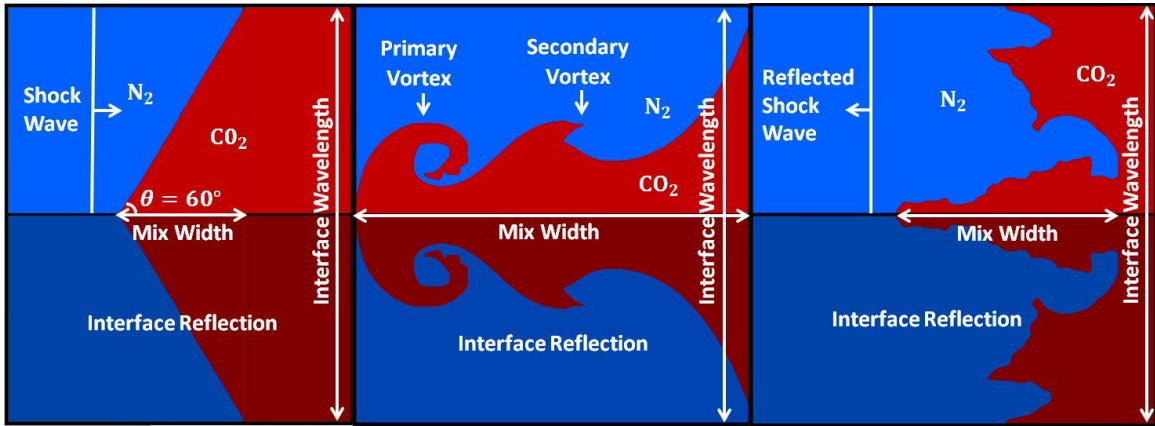
Figure 28: Inclined interface mixing width and wavelength with interface reflection.

This results in one full wavelength, which is periodic when taking the fast Fourier Transform (FFT). The energy spectra components were computed by taking the FFT of each row in the spanwise direction and multiplying it by its complex conjugate as shown in equations (4.10) and (4.11).

$$[E_{u'}]_i = FFT([K_{u'}]_i) \cdot conj(FFT([K_{u'}]_i)) \qquad (4.8)$$

69

$$[E_{v'}]_i = FFT([K_{v'}]_i) \cdot conj(FFT([K_{v'}]_i)) \qquad (4.9)$$

where $[E_{u'}]_i$ is the u' component of the energy spectra for the ith row. The u' and v' components of TKE are given by

$$K_{u'} = \frac{1}{2}\overline{u'} \qquad (4.10)$$

$$K_{v'} = \frac{1}{2}\overline{v'} \qquad (4.11)$$

where u' and v' are the x- and y-components of the fluctuation velocities, respectively. The velocity fluctuations were not squared in equations (4.10) and (4.11) because they are squared in equations (4.8) and (4.9). The energy spectra was calculated by adding the u' and v' components.

$$[E]_i = [E_{u'}]_i + [E_{v'}]_i \qquad (4.12)$$

After the energy spectra was averaged across all the rows, only the first half was retained due to the Nyquist sampling frequency restraint. This procedure was performed on ten experimental sets of data per case; thus, the overall average used 4,340 rows of data.

The spectra for the experimental data sets are shown in . In the majority of cases, the spectra show two decades of spread at the small wavenumbers, but begin to collapse

70

at wavenumbers larger than 1000 m^{-1}. Moreover, the largest wavenumber is related to the smallest measureable wavelength, which is 480 μm. A large amount of energy is present at low wavenumbers because of the large length scale of the inclined interface perturbation. In Case 3 post-reshock, large structures collapse as energy migrates to smaller scales.

The experimental runs for each case before and after reshock were ensemble averaged together to allow for easier comparison within and between cases. Once the runs were averaged together the spectra were non-dimensionalized by normalizing the energy spectra with respect to its peak value and the wave number with respect to the Kolmogorov scale. The Kolmogorov scale that was used to non-dimensionalize the wave number was calculated based on the mixing width growth rate since the interface length was not an accurate measure for Case 3.
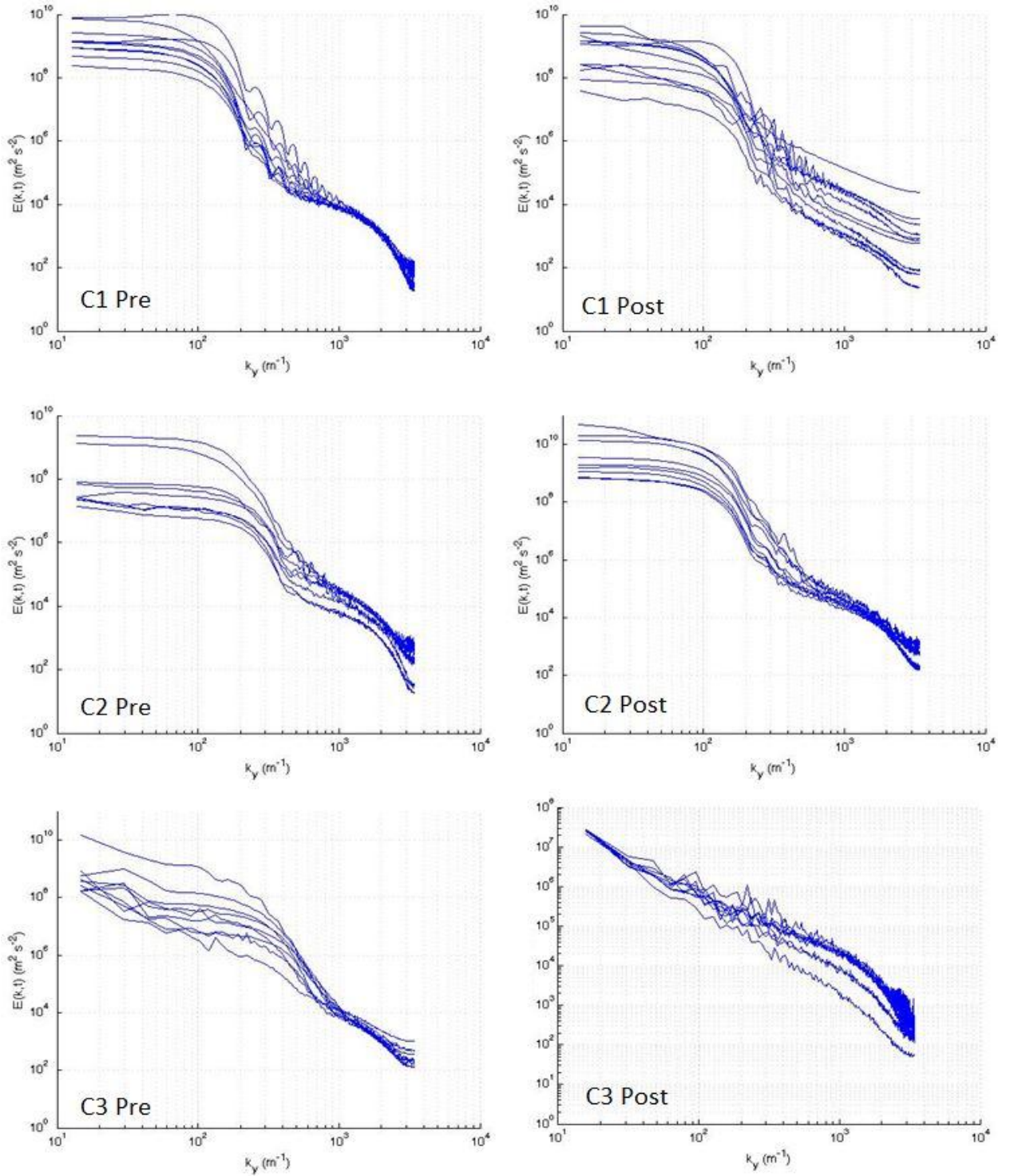
Figure 29: Ten runs of TKE spectra for each case for before (left column) and after (second column above) reshock. In some case, less than ten runs were reported because outliers were removed.

Figure 30 shows the ensemble-averaged spectra for Case 1 before and after reshock with Mie scattering images for reference. The spectra show that the pre-reshock interface carries its turbutlent kinetic energy in larger scales that the post-reshock interface since the pre-reshock spectra is located in a lower wavenumber region. This is supported when the structures in the pre- and post-reshock Mie scattering images are compared and the post-reshock interface possesses smaller scale features. This increase in small scale features also provides and explanation of the increased energy at high wavenumbers for the post-reshock interface. As the interface is compressed by the reshock wave, the mixing width decreases which causes a similar decrease of the Kolmogorov scale of the field. When the spectra are normalized by the Kolmogorov scale, the difference in the normalization factor causes the difference in horizontal location between the spectra providing a clear description of the scales present in the flow.

Figure 30: Case 1 ensemble-averaged, normalized TKE spectra before and after reshock. Mie scattering images included for reference.

Figure 31 shows the ensemble-averaged spectra for Case 2 before and after reshock. In this case, the spectra show very similar behavior but are separated due to the difference in the Kolmogorov scale before and after reshock. The energy distribution in the post-reshock case can be explained by looking at the well-defined structures of the corresponding Mie scattering image. In the post-reshock image, well-defined structures that are of comparable size to the primary vortex structure pre-reshock as well as small scale features that are developing in conjunction with the larger structures.
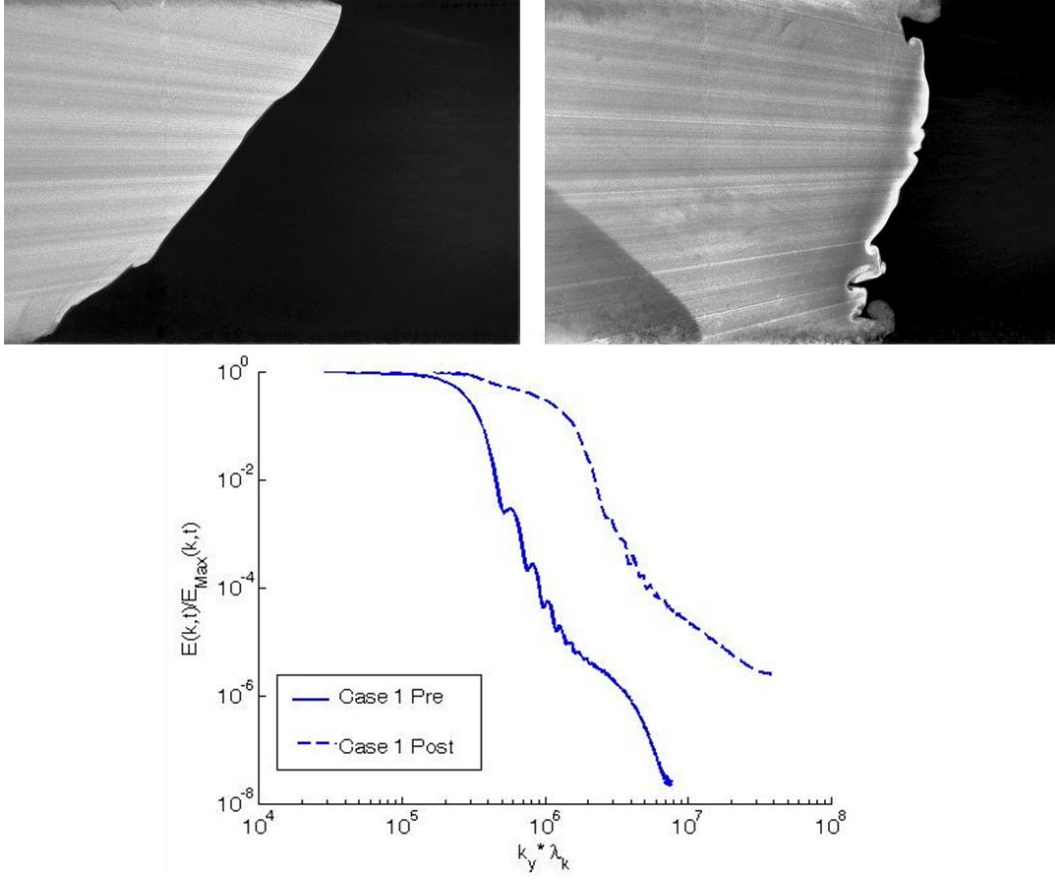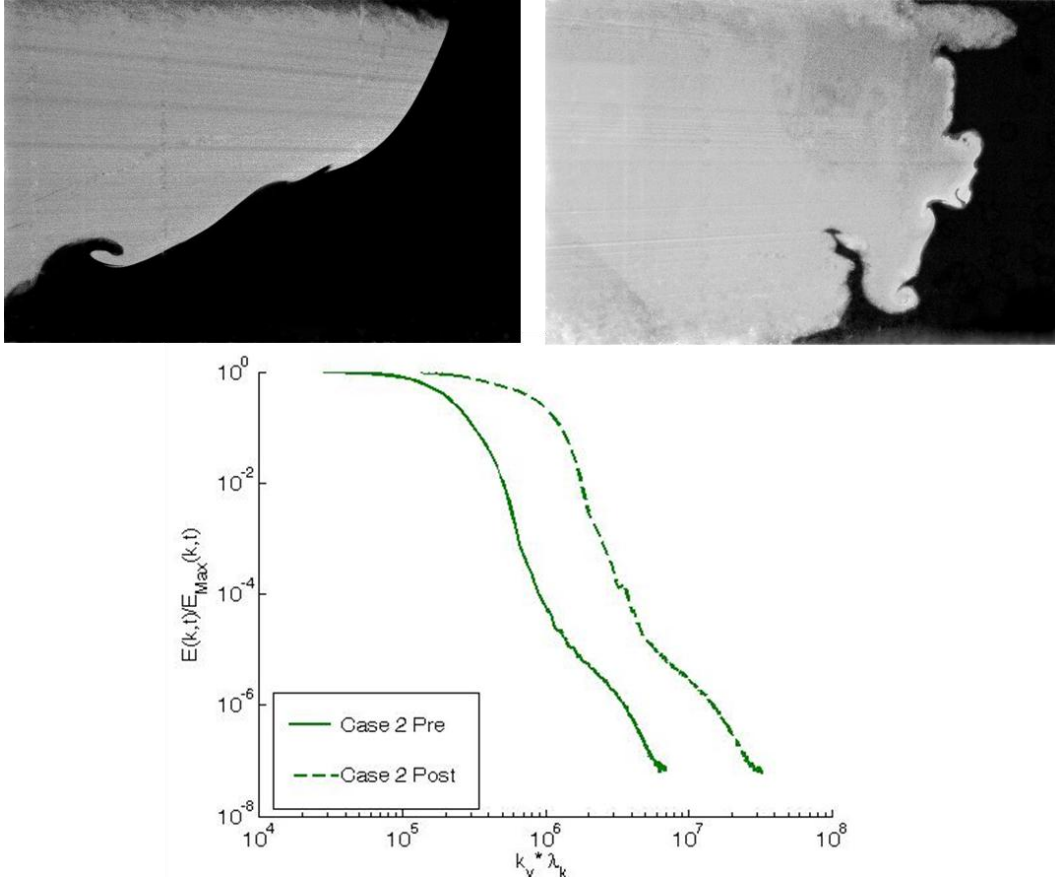
Figure 31: Case 2 ensemble-average, normalized TKE spectra before and after reshock. Mie scattering images included for reference.

The normalized, ensemble-averaged spectra for Case 3 before and after reshock are shown in Figure 32. Unlike the other cases, the spectra for Case 3 immediately begin to slope downward rather than being constant at the smallest wavenumbers, which shows that there is more energy being carried by the smaller structures in the flow field. The increased energy at larger wavenumbers for the post-reshock spectra is in line with the scales of structures seen in the Mie scattering images. The post-reshock Mie scattering image shows no larger, coherent structures present and an interface that has become dominated by smaller scales. Similarly there is a larger portion of the total

energy of the flow field present in the smaller scales in the spectra. The $k^{-5/3}$ power

decay is plotted for reference and the post-reshock spectrum for case 3 seems to follow

this trend, which is a sign of classical turbulence in the flow field from the

Kolmogorov's hypothesis.
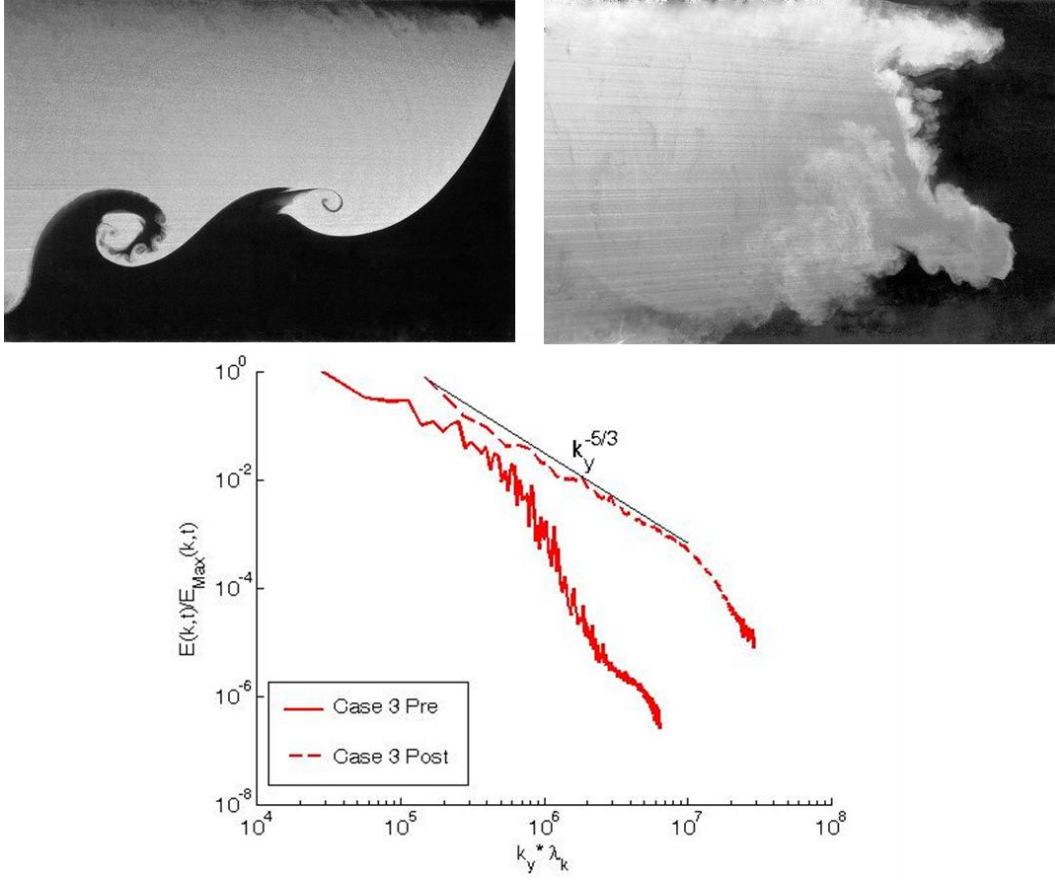
Figure 32: Case 3 ensemble-averaged, normalized TKE spectra before and after reshock. Mie scattering images and k$^{-5/3}$ decay included for reference.

The pre- and post-reshock turbulent kinetic energy spectra for the three cases are

compared in Figure 33, parts A and B respectively. Examining first the pre-reshock

spectra, the overall behavior of the spectra for Cases 1 and 2 are very similar for medium

to large wavenumbers. The Case 2 spectrum extends to smaller wavenumbers than Case

1 which is supported by the larger scale structures that are present in the Case 2 pre-reshock interface than its Case 1 counterpart. Case 3 shows different behavior, beginning at a similar small wavenumber to Case 2 but carrying more energy in the medium to large wavenumbers than the other cases. This can also be seen in the Mie scattering image for Case 3 pre-reshock where while there are large vortex structures, the presence of the smaller secondary Kelvin-Helmholtz instability roll-ups indicates that a portion of the energy will be carried at these smaller scales. A similar relation between the three cases can be seen post-reshock as well.

The spectra for Cases 1 and 2 post-reshock show a large portion of the total energy being carried at the smaller wavenumbers with Case 2 being shifted slightly towards the lower wavenumbers. Case 3 shows a steady decline without indication of a large concentration of energy in a small range of small wavenumbers like the other cases. Figure 34 compares the spectra for all three cases before and after reshock. In all cases, the post-reshock spectra are at larger wavenumbers than their pre-reshock counterparts. This shift is cause by the disintegration of the large-scale structures of the pre-reshock interfaces by the deposition of baroclinic torque by the reshock wave. The disintegration of large-scale, coherent structures allows for the smaller scales to being to dominate the flow field and carry more of the flows energy.

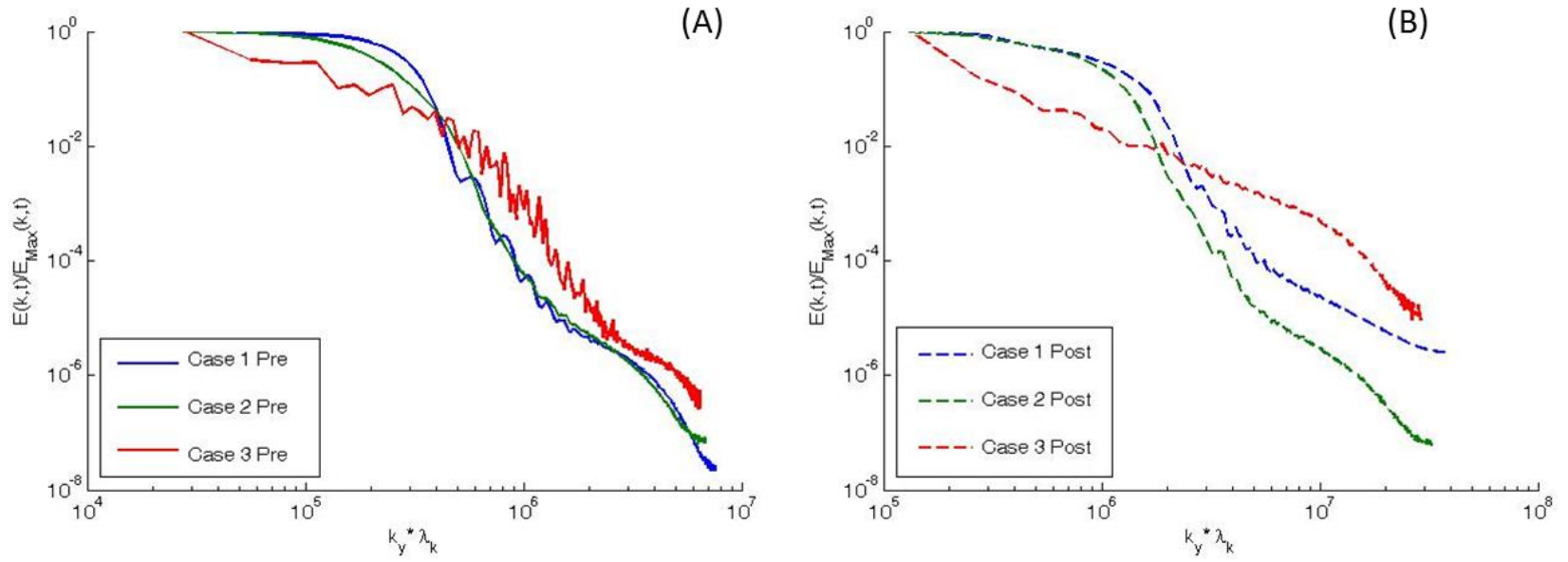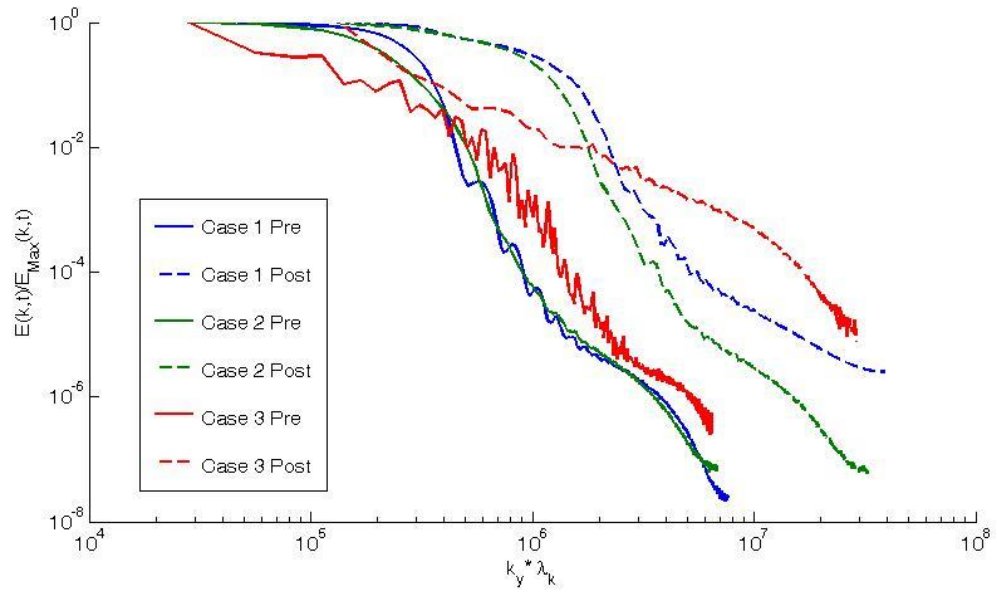**Figure 33: Pre- (A) and post-reshock (B) TKE spectra comparison.**

Figure 34: Ensemble-averaged, normalized TKE for all three cases before and after reshock.

5. CONCLUSIONS

Mie scattering image series for each of the three cases were presented. Analysis of the image series for each experimental case showed that the larger and more distributed the vortex structures pre-reshock, the greater the mixing in the post-reshock flow field because the structures present in the interface pre-reshock are destroyed by the reshock wave and dissipated to smaller scales. Present in the Mie scattering images and the vorticity plots, a slip line is formed up stream of the reshocked interface. The slip line is a lambda shock leg created when the reshock wave reflection, reflected off of the interface and the bottom wall of the shock tube, interacts with the transmitted reshock wave. The mixing width growth rate measured experimentally was in very good agreement with the simulation predicted values and showed that in all three cases the interface mixing width compresses at similar speeds, approximately 84 m/s, 92 m/s and 98 m/s for Case 1, 2 and 3 respectively. The interface length showed very different growth rates for the three experimental cases with Cases 1 and 2 the interface showed lengthening of the interface and Case 3 showing a contraction of interface length. This contraction is a product of the collapse and mixing of the prior vortex structure. This illustrates a short-coming of the interface length measure for determining interface growth.

Particle image veloctimetry was used to measure the flow field velocity for all three cases and the velocity data was used to calculate vorticity, enstrophy, circulation and turbulent kinetic energy. The vorticity of the interface is found to change direction after the reshock interaction due to the additional application of baroclinic torque by the

reshock wave. In Case 2 and 3, the large vortex structures cause the interface to retain some pockets of negative vorticity. These pockets indicate that Case 2 has memory of the pre-reshock conditions but in Case 3, the vorticity plot shows a very complex field that indicates a very well mixed flow field with no memory of the pre-reshock conditions.

The sum of the enstrophy for the flow field was calculated and showed that the more developed experimental cases showed higher enstrophy post-reshock. The enstrophy data from the experiments did not agree with the simulation and the disagreement could be caused by differences in resolution between the experiments and simulations. The experimental circulation results show that the more developed the interface is before reshock the larger the magnitude of circulation deposited by the reshock wave. The experimentally calculated circulation was also compared to the simulation predicted circulation and the total circulation values show good agreement with the results but the positive and negative circulation components do not.

Using the two growth rates and the circulation, Reynolds numbers for the flow can be calculated and used to determine the turbulent length scales that pertain to the flow field. The Kolmogorov length scale and the Taylor microscale were calculated for four different Reynolds numbers, for each case before and after reshock. The post-reshock scales show that the Kolmogorov scale is two orders of magnitude below our experimental resolution and the Taylor microscale is on the same order as the experimental resolution. These show that the experiments do not capture any mixing on the Kolmogorov scale but the experiments may capture the inertial subrange mixing.

Turbulent kinetic energy spectra for the experiments and the results showed good agreement within each case. The individual spectra for each were ensemble-averaged together to produce a single spectrum for each case before and after reshock and then normalized with respect to the peak energy and Kolmogorov scale for each spectrum. The spectra show that the energy of the flow field post-reshock is carried at smaller scales than pre-reshock for all cases and that the post-reshock spectrum for Case 3 appears to have reached a turbulent state by approaching a $k^{-5/3}$ power law decay, a sign of classical turbulence from Kolmogorov's hypothesis.

Future experimental work would be to expand the current work to different Atwood numbers, Mach numbers and inclination angles to investigate the effect of each on circulation deposition and TKE. Diagnostic additions to the experimental facility would include in implementation of acetone planar laser induced florescence (PLIF) to record density data and simultaneous PLIF and PIV will allow for more advance turbulence statistics to be calculated. Also, current and future experimental work can be compared to the three-dimensional ARES simulations that are currently being developed by Dr. McFarland in conjunction with Lawrence Livermore National Laboratory.

REFERENCES

[1] E. E. Meshkov, "Instability of the Interface of Two Gases Accelerated by a Shock Wave," *Fluid Dyn.*, vol. 4, no. 5, pp. 101–104, Sep. 1969.

[2] R. D. Richtmyer, "Taylor Instability in Shock Acceleration of Compressible Fluids," *Commun. Pure Appl. Math.*, vol. 13, no. 2, pp. 297–319, 1960.

[3] J. W. S. Rayleigh, "Investigation of the Character of the Equilibrium of an Incompressible Heavy Fluid of Variable Density," *Proc. Lond. Math. Soc.*, vol. 14, pp. 170–177, 1883.

[4] G. Taylor, "The Instability of Liquid Surfaces when Accelerated in a Direction Perpendicular to their Planes. I," *Proc. R. Soc. Lond. Ser. Math. Phys. Sci.*, vol. 201, no. 1065, pp. 192–196, Mar. 1950.

[5] W. Kelvin, "XLVI. Hydrokinetic Solutions and Observations," *Philos. Mag. Ser. 4*, vol. 42, no. 281, pp. 362–377, 1871.

[6] Helmholtz, "XLIII. On discontinuous Movements of Fluids," *Philos. Mag. Ser. 4*, vol. 36, no. 244, pp. 337–346, 1868.

[7] K. A. Meyer and P. J. Blewett, "Numerical Investigation of the Stability of a Shock-Accelerated Interface between Two Fluids," *Phys. Fluids 1958-1988*, vol. 15, no. 5, pp. 753–759, Aug. 2003.

[8] G. Fraley, "Rayleigh–Taylor Stability for a Normal Shock Wave–Density Discontinuity Interaction," *Phys. Fluids 1958-1988*, vol. 29, no. 2, pp. 376–386, Feb. 1986.

[9] J. Wouchuk, "Growth Rate of the Linear Richtmyer-Meshkov Instability When a Shock is Reflected," *Phys. Rev. E*, vol. 63, no. 5, Apr. 2001.

[10] J. G. Wouchuk and K. Nishihara, "Asymptotic Growth in the Linear Richtmyer–Meshkov Instability," *Phys. Plasmas 1994-Present*, vol. 4, no. 4, pp. 1028–1038, Apr. 1997.

[11] J. G. Wouchuk and K. Nishihara, "Linear Perturbation Growth at a Shocked Interface," *Phys. Plasmas 1994-Present*, vol. 3, no. 10, pp. 3761–3776, Oct. 1996.

[12] M. Vandenboomgaerde, C. Mügler, and S. Gauthier, "Impulsive Model for the Richtmyer-Meshkov Instability," *Phys. Rev. E*, vol. 58, no. 2, pp. 1874–1882, Aug. 1998.

[13] B. Motl, J. Oakley, D. Ranjan, C. Weber, M. Anderson, and R. Bonazza, "Experimental Validation of a Richtmyer–Meshkov Scaling Law Over Large Density Ratio and Shock Strength Ranges," *Phys. Fluids 1994-Present*, vol. 21, no. 12, p. 126102, Dec. 2009.

[14] M. Brouillette and B. Sturtevant, "Experiments on the Richtmyer–Meshkov Instability: Single-scale Perturbations on a Continuous Interface," *J. Fluid Mech.*, vol. 263, pp. 271–292, 1994.

[15] M. Brouillette, "The Richtmyer-Meshkov Instability," *Annu. Rev. Fluid Mech.*, vol. 34, no. 1, pp. 445–468, 2002.

[16] A. N. Aleshin, E. G. Gamalii, S. G. Zaitsev, E. V. Lazareva, and I. G. Lebo, "A Study of the Nonlinear and Transition Stages of the Evolution of the Richtmyer-Meshkov Instability," *Pisma V Zhurnal Tekhnischeskoi Fiz.*, vol. 14, pp. 1063–1067, Jun. 1988.

[17] J. A. McFarland, J. A. Greenough, and D. Ranjan, "Computational Parametric Study of a Richtmyer-Meshkov Instability for an Inclined Interface," *Phys. Rev. E*, vol. 84, no. 2, Aug. 2011.

[18] Q. Zhang and S.-I. Sohn, "An Analytical Nonlinear Theory of Richtmyer-Meshkov Instability," *Phys. Lett. A*, vol. 212, no. 3, pp. 149–155, 1996.

[19] A. L. Velikovich and G. Dimonte, "Nonlinear Perturbation Theory of the Incompressible Richtmyer-Meshkov Instability," *Phys. Rev. Lett.*, vol. 76, no. 17, pp. 3112–3115, Apr. 1996.

[20] R. L. Holmes, G. Dimonte, B. Fryxell, M. L. Gittings, J. W. Grove, M. Schneider, D. H. Sharp, A. L. Velikovich, R. P. Weaver, and Q. Zhang, "Richtmyer–Meshkov Instability Growth: Experiment, Simulation and Theory," *J. Fluid Mech.*, vol. 389, pp. 55–79, 1999.

[21] K. O. Mikaelian, "Richtmyer-Meshkov Instabilities in Stratified Fluids," *Phys. Rev. A*, vol. 31, no. 1, pp. 410–419, Jan. 1985.

[22] K. O. Mikaelian, "Turbulent Mixing Generated by Rayleigh-Taylor and Richtmyer-Meshkov Instabilities," *Phys. Nonlinear Phenom.*, vol. 36, no. 3, pp. 343–357, Aug. 1989.

[23] H. F. Robey, P. M. Celliers, J. L. Kline, A. J. Mackinnon, T. R. Boehly, O. L. Landen, J. H. Eggert, D. Hicks, S. Le Pape, D. R. Farley, M. W. Bowers, K. G. Krauter, D. H. Munro, O. S. Jones, J. L. Milovich, D. Clark, B. K. Spears, R. P. J. Town, S. W. Haan, S. Dixit, M. B. Schneider, E. L. Dewald, K. Widmann, J. D. Moody, T. D. Döppner, H. B. Radousky, A. Nikroo, J. J. Kroll, A. V. Hamza, J. B.

Horner, S. D. Bhandarkar, E. Dzenitis, E. Alger, E. Giraldez, C. Castro, K. Moreno, C. Haynam, K. N. LaFortune, C. Widmayer, M. Shaw, K. Jancaitis, T. Parham, D. M. Holunga, C. F. Walters, B. Haid, T. Malsbury, D. Trummer, K. R. Coffee, B. Burr, L. V. Berzins, C. Choate, S. J. Brereton, S. Azevedo, H. Chandrasekaran, S. Glenzer, J. A. Caggiano, J. P. Knauer, J. A. Frenje, D. T. Casey, M. Gatu Johnson, F. H. Séguin, B. K. Young, M. J. Edwards, B. M. Van Wonterghem, J. Kilkenny, B. J. MacGowan, J. Atherton, J. D. Lindl, D. D. Meyerhofer, and E. Moses, "Precision Shock Tuning on the National Ignition Facility," *Phys. Rev. Lett.*, vol. 108, no. 21, p. 215004, May 2012.

[24] C. C. Kuranz, R. P. Drake, E. C. Harding, M. J. Grosskopf, H. F. Robey, B. A. Remington, M. J. Edwards, A. R. Miles, T. S. Perry, B. E. Blue, T. Plewa, N. C. Hearn, J. P. Knauer, D. Arnett, and D. R. Leibrandt, "Two-Dimensional Blast-Wave-Driven Rayleigh-Taylor Instability: Experiment and Simulation," *Astrophys. J.*, vol. 696, no. 1, p. 749, May 2009.

[25] O. A. Hurricane, J. F. Hansen, E. C. Harding, V. A. Smalyuk, B. A. Remington, G. Langstaff, H.-S. Park, H. F. Robey, C. C. Kuranz, M. J. Grosskopf, and R. S. Gillespie, "Blast-wave Driven Kelvin-Helmholtz Shear Layers in a Laser Driven High-Energy-Density Plasma," *Astrophys. Space Sci.*, vol. 336, no. 1, pp. 139–143, Nov. 2011.

[26] B. Blue, S. Weber, S. Glendinning, N. Lanier, D. Woods, M. Bono, S. Dixit, C. Haynam, J. Holder, D. Kalantar, B. MacGowan, A. Nikitin, V. Rekow, B. Van Wonterghem, E. Moses, P. Stry, B. Wilde, W. Hsing, and H. Robey, "Experimental Investigation of High-Mach-Number 3D Hydrodynamic Jets at the National Ignition Facility," *Phys. Rev. Lett.*, vol. 94, no. 9, Mar. 2005.

[27] P. R. Chapman and J. W. Jacobs, "Experiments on the Three-Dimensional Incompressible Richtmyer-Meshkov Instability," *Phys. Fluids 1994-Present*, vol. 18, no. 7, p. 074101, Jul. 2006.

[28] K. I. Read, "Experimental Investigation of Turbulent Mixing by Rayleigh-Taylor Instability," *Phys. Nonlinear Phenom.*, vol. 12, no. 1–3, pp. 45–58, Jul. 1984.

[29] N. Yamashita and J. W. Jacobs, "The Experimental Study of Rayleigh-Taylor Instability using a Linear Induction Motor Accelerator," *Bull. Am. Phys. Soc.*, vol. 54, 2009.

[30] J. W. Jacobs and I. Catton, "Three-dimensional Rayleigh-Taylor Instability Part 2. Experiment," *J. Fluid Mech.*, vol. 187, pp. 353–371, 1988.

[31] M. Vetter and B. Sturtevant, "Experiments on the Richtmyer-Meshkov Instability of an Air/SF6 Interface," *Shock Waves*, vol. 4, no. 5, pp. 247–252, Mar. 1995.

[32] C. Bailie, J. A. McFarland, J. A. Greenough, and D. Ranjan, "Effect of Incident Shock Wave Strength on the Decay of Richtmyer–Meshkov Instability-Introduced Perturbations in the Refracted Shock Wave," *Shock Waves*, vol. 22, no. 6, pp. 511–519, Nov. 2012.

[33] E. Leinov, O. Sadot, A. Formoza, G. Malamud, Y. Elbaz, L. A. Levin, G. Ben-Dor, and D. Shvarts, "Investigation of the Richtmyer–Meshkov Instability Under Re-shock Conditions," *Phys. Scr.*, vol. 2008, no. T132, p. 014014, Dec. 2008.

[34] D. Ranjan, J. H. J. Niederhaus, J. G. Oakley, M. H. Anderson, J. A. Greenough, and R. Bonazza, "Experimental and Numerical Investigation of Shock-Induced Distortion of a Spherical Gas Inhomogeneity," *Phys. Scr.*, vol. T132, p. 014020, Dec. 2008.

[35] R. Bonazza and B. Sturtevant, "X-ray Measurements of Growth Rates at a Gas Interface Accelerated by Shock Waves," *Phys. Fluids*, vol. 8, no. 9, p. 2496, 1996.

[36] J. W. Jacobs, "Shock-induced Mixing of a Light-Gas Cylinder," *J. Fluid Mech.*, vol. 234, pp. 629–649, 1992.

[37] S. Balasubramanian, G. C. Orlicz, K. P. Prestridge, and B. J. Balakumar, "Experimental Study of Initial Condition Dependence on Richtmyer-Meshkov Instability in the Presence of Reshock," *Phys. Fluids 1994-Present*, vol. 24, no. 3, p. 034103, Mar. 2012.

[38] B. D. Collins and J. W. Jacobs, "PLIF Flow Visualization and Measurements of the Richtmyer–Meshkov Instability of an Air/SF6 Interface," *J. Fluid Mech.*, vol. 464, pp. 113–136, 2002.

[39] C. Weber, N. Haehn, J. Oakley, D. Rothamer, and R. Bonazza, "Turbulent Mixing Measurements in the Richtmyer-Meshkov Instability," *Phys. Fluids 1994-Present*, vol. 24, no. 7, p. 074105, Jul. 2012.

[40] J. A. McFarland, "Experimental and Computational Study of the Inclined Interface Richtmyer-Meshkov Instability," Doctoral Dissertation, Texas A&M University, 2013.

[41] R. Samtaney and N. J. Zabusky, "On Shock Polar Analysis and Analytical Expressions for Vorticity Deposition in Shock-Accelerated Density-Stratified Interfaces," *Phys. Fluids Fluid Dyn.*, vol. 5, p. 1285, 1993.

[42] R. Samtaney and N. J. Zabusky, "Circulation Deposition on Shock-Accelerated Planar and Curved Density-Stratified Interfaces: Models and Scaling Laws," *J. Fluid Mech.*, vol. 269, no. 45–78, p. 2, 1994.

[43] "Shock Tube Experiments on Richtmyer-Meshkov Instability across a Chevron Profiled Interface," presented at the 8th International Workshop on the Physics of Compressible Turbulent Mixing, Pasadena, CA, 2001.

[44] J. Liu, D. Tan, W. Huang, and L. Zou, "Experiments on the Growth Rate of Single and Two Modes RM Instability by Re-shock."

[45] B. J. Balakumar, G. C. Orlicz, C. D. Tomkins, and K. P. Prestridge, "Simultaneous Particle-Image Velocimetry–Planar Laser-Induced Fluorescence Measurements of Richtmyer–Meshkov Instability Growth in a Gas Curtain With and Without Reshock," *Phys. Fluids*, vol. 20, no. 12, p. 124103, Dec. 2008.

[46] B. Thornber, D. Drikakis, D. L. Youngs, and R. J. R. Williams, "Growth of a Richtmyer-Meshkov Turbulent Layer After Reshock," *Phys. Fluids*, vol. 23, no. 9, p. 095107, Sep. 2011.

[47] C. Weber, N. Haehn, J. Oakley, M. Anderson, and R. Bonazza, "Richtmyer-Meshkov Experiments on a Reshocked, Low Atwood Number Interface," in *Bulletin of the American Physical Society*, 2008, vol. Volume 53, Number 15.

[48] C. Weber, N. Haehn, J. Oakley, M. Anderson, and R. Bonazza, "Richtmyer–Meshkov Instability on a Low Atwood Number Interface After Reshock," *Shock Waves*, vol. 22, no. 4, pp. 317–325, Jul. 2012.

[49] M. Latini, O. Schilling, and W. S. Don, "Effects of WENO Flux Reconstruction Order and Spatial Resolution on Reshocked Two-Dimensional Richtmyer–Meshkov Instability," *J. Comput. Phys.*, vol. 221, no. 2, pp. 805–836, Feb. 2007.

[50] O. Schilling, M. Latini, and W. Don, "Physics of Reshock and Mixing in Single-Mode Richtmyer-Meshkov Instability," *Phys. Rev. E*, vol. 76, no. 2, Aug. 2007.

[51] M. Lombardini, D. J. Hill, D. I. Pullin, and D. I. Meiron, "Atwood Ratio Dependence of Richtmyer–Meshkov Flows under Reshock Conditions Using Large-eddy Simulations," *J. Fluid Mech.*, vol. 670, pp. 439–480, Feb. 2011.

[52] D. J. Hill, C. Pantano, and D. I. Pullin, "Large-eddy Simulation and Multiscale Modelling of a Richtmyer–Meshkov Instability with Reshock," *J. Fluid Mech.*, vol. 557, pp. 29–61, 2006.

[53] D. Arnett, "The Role of Mixing in Astrophysics," *Astrophys. J. Suppl. Ser.*, vol. 127, no. 2, p. 213, Apr. 2000.

[54] J. Krebs and W. Hillebrandt, "The Interaction of Supernova Shockfronts and Nearby Interstellar Clouds," *Astron. Astrophys.*, vol. 128, pp. 411–419, Dec. 1983.

[55] R. I. Klein, C. F. McKee, and P. Colella, "On the Hydrodynamic Interaction of the Shock Waves with Interstellar Clouds. 1: Nonradiative Shocks in Small Clouds," *Astrophys. J. Part 1*, vol. 420, no. 1, pp. 213–236.

[56] F. Marble, E. Zukoski, J. Jacobs, and G. Hendricks, "Shock Enhancement and Control of Hypersonic Mixing and Combustion," in *26th Joint Propulsion Conference*, American Institute of Aeronautics and Astronautics.

[57] J. Yang, T. Kubota, and E. E. Zukoski, "Applications of Shock-Induced Mixing to Supersonic Combustion," *AIAA J.*, vol. 31, no. 5, pp. 854–862, 1993.

[58] F. Houwing, A. Bishop, M. Gaston, J. Fox, P. Danehy, and N. Mudford, "Simulated Fuel-Jet/Shock-Wave Interaction," in *Proceedings of 23rd International Symposium on Shock Waves, Fort Worth, Texas, Published by The University of Texas at Arlington, Arlington, Texas, USA.(CD ROM)*, 2001, pp. 1074–1080.

[59] M. Delius, "Medical Applications and Bioeffects of Extracorporeal," *Shock Waves*, vol. 4, no. 2, pp. 55–72, Sep. 1994.

[60] J. D. Lindl, R. L. McCrory, and E. M. Campbell, "Progress Toward Ignition and Burn Propagation in Inertial Confinement Fusion," *Phys. Today*, vol. 45, p. 32, 1992.

[61] J. A. McFarland, J. A. Greenough, and D. Ranjan, "Investigation of the Initial Perturbation Amplitude for the Inclined Interface Richtmyer–Meshkov Instability," *Phys. Scr.*, vol. 2013, no. T155, p. 014014, Jul. 2013.

[62] J. A. McFarland, D. Ranjan, and J. A. Greenough, "Simulations and Analysis of Shock Accelerated Inhomogenous Flows With and Without Reshock," pp. 1047–1053, Jul. 2012.

[63] S. Kumar, G. Orlicz, C. Tomkins, C. Goodenough, K. Prestridge, P. Vorobieff, and R. Benjamin, "Stretching of Material Lines in Shock-Accelerated Gaseous Flows," *Phys. Fluids 1994-Present*, vol. 17, no. 8, p. 082107, Aug. 2005.